Mathematical and computational modelling of vegetated soil incorporating hydraulically-driven finite strain deformation

Woodman, N. D.; Smethurst, J. A.; Roose, T.; Powrie, W.; Meijer, Gerrit; Knappett, Jonathan

Published in:
Computers and Geotechnics

DOI:
10.1016/j.compgeo.2020.103754

Publication date:
2020

Mathematical and computational modelling of vegetated soil incorporating hydraulically-driven finite strain deformation.

Woodman, N.D.[1*], Smethurst J.A.[1], Roose, T.[1], Powrie, W[1], Meijer, G. J.[2], Knappett, J.A.[2], Dias, T.[1]

*Corresponding Author

[1.] Faculty of Engineering and Physical Sciences, University of Southampton, Highfield, Southampton, SO17 1BJ, United Kingdom

[2.] School of Science and Engineering, University of Dundee, Dundee, DD1 4HN, United Kingdom.

n.d.woodman@soton.ac.uk, j.a.smethurst@soton.ac.uk, T.Roose@soton.ac.uk, W.Powrie@soton.ac.uk, g.j.z.meijer@dundee.ac.uk, j.a.Knappett@dundee.ac.uk, T.Gerheim-Souza-Dias@southampton.ac.uk

Keywords: Slope, vegetated soil, roots, landslide, large-strain

Nomenclature

Acronyms

MCC- Modified Cam-Clay, ET – Evapotranspiration, LE – linear Elastic, RWU – root water uptake.

Symbols

α	Soil moisture retention parameter (1/m)
ε	Eulerian-Almansi Strain (-)
$\delta\varepsilon_d$	Deviator strain increment $= \frac{1}{3}\left\{2\left[\left(\delta\varepsilon_{22}-\delta\varepsilon_{33}\right)^2+\left(\delta\varepsilon_{33}-\delta\varepsilon_{11}\right)^2+\left(\delta\varepsilon_{11}-\delta\varepsilon_{22}\right)^2\right]+3(\delta\varepsilon_{23}^2+\delta\varepsilon_{31}^2+\delta\varepsilon_{12}^2)\right\}^{1/2}$
η	Stress ratio $= q/p'$
$\boldsymbol{\Gamma}$	External boundary of the model (m)
κ^2	Ratio of axial to radial conductance (-)
κ	Slope of the Modified Cam-Clay unloading-reloading line in the v:ln p' plane (-)
λ	Slope of the Modified Cam-Clay normal compression line in the v:ln p' plane (-)
μ	Viscosity of water (cP)
μ_a	Viscosity of air (cP)s
ν	Poisson's ratio (-)
ρ	Density of water (kg/m^3)
ρ_a	Density of air (kg/m^3)
ρ_s	Density of soil solid grains (kg/m^3)
$\boldsymbol{\sigma}$	Cauchy Stress (Pa)
$\boldsymbol{\sigma}'$	Effective Cauchy Stress (Pa)
$\boldsymbol{\sigma_r}$	Root stress tensor (Pa)
ϕ	Volume fraction (-)
$\phi_{s,i}$	Initial solid volume fraction (-)
χ	Effective stress parameter (-)

A	Cross-sectional area (m^2)
a	Root radius (m)
$\boldsymbol{C}$	Elasticity tensor (-)
D	Domain height (m)
e	Void ratio (-)
E	Young's Modulus (Pa)
$\boldsymbol{F}$	Deformation-gradient tensor (m/m)
F_R	Sink term due to root water uptake (RWU) (1/s)
$\boldsymbol{f_V}$	Body force per unit volume (N/m^3)
g	Acceleration due to gradity (m/s^2)
G	Shear modulus (Pa)
I	Identity matrix (-)
$\hat{\boldsymbol{\imath}}$	Lateral (x) unit vector (-)
J	Jacobian determinant (-)
$\hat{\boldsymbol{\jmath}}$	Lateral (y) unit vector (-)

k_w Permeability to water (m^2)
K Bulk modulus (Pa)
K_0 Ratio of horizontal to vertical effective stress (-)
K_s Saturated hydraulic conductivity (m/s)
k_a Permeability to air (m^2)
k Intrinsic permeability (m^2)
k_0 Reference intrinsic permeability for Kozeny-Carman relationship (m^2)
$\widehat{\boldsymbol{k}}$ Vertical (z) unit vertical vector (-)
k_R Root radial conductivity (m/Pa/s)
k_z Root axial conductivity (m^4/Pa/s)
L_R Length of root (m)
L Exponent for K (-)
l_d Root length density (m/m^3)
M Exponent in water retention relationship (-)
M Slope of critical state line.
N Exponent in water retention relationship (-)
n_i Number of roots of given radius (-)
P Root base pressure (MPa)
p Pressure (air or water) (Pa)
p' Mean effective stress (Pa)
p'_{pc} Pre-consolidation pressure (Pa)
p_a Air pressure (Pa)
p_{atm} Atmospheric pressure (Pa)
p_R Water pressure within the root xylem (Pa)
q Deviator stress $= \left[\frac{(\sigma'_{22}-\sigma'_{33})^2+(\sigma'_{33}-\sigma'_{11})^2+(\sigma'_{11}-\sigma'_{22})^2}{2} + 3(\sigma'^2_{23}+\sigma'^2_{31}+\sigma'^2_{12})\right]^{1/2}$ (Pa)
R_i Radius of xylem tube (m)
R Rainfall rate (m/d)
S_w Water saturation (-)
t Time (d)
$\boldsymbol{u}$ Displacement vector (m)
v Specific volume (-)
$\boldsymbol{v}$ Velocity of (m/s)
$\mathbf{X}$ Material co-ordinate vector (m)
$\boldsymbol{x}$ Spatial coordinate vector (m)
z Vertical dimension (m)

Subscripts

0 Reference, initial
a Air
e Elastic
f Fluid (air plus water)
p Plastic
s Solid
so Soil
w Water

1 Introduction

The role of plant roots is increasingly being included in geotechnical assessment of unsaturated or partly-saturated[1] vegetated slopes [1]; [2]; [3]; [4], and is specifically incorporated into 'bio-engineering' design for slope performance [5]; [6]; [7]; [8]; [9]; [10]. Vegetation can influence ground movements (*e.g.* seasonal shrinkage and swelling of soils) and increase the stability slopes through both the generation of pore water suctions and mechanical reinforcing action of the roots.

Field and laboratory experiments have demonstrated the mechanical reinforcement effects of plant roots on slopes [11]; [12], with roots able to increase significantly the apparent shear resistance of the host soil [13]; [14]; [15]. Relatively thick woody roots are able to withstand bending moments and can act as 'soil nails' [9], while thinner more flexible roots can provide tensional reinforcement. In taking up water from the soil, plant roots can develop pore water suctions up to 1.5 MPa, increasing the effective direct soil stresses substantially [11]. Pore water pressure changes transmit beyond the rooting zone, effectively extending the influence of the roots to greater depths and thereby influencing more deep-seated failure mechanisms [16]; [4]. In [17] it was demonstrated that the trees growing on earthworks can maintain pore water suctions beneficial to slope stability, particularly during the winter months in a temperate climate, when transpiration is low and rainfall high. In [18] and [19] researchers measured vertical ground surface displacements of several centimetres in clay railway embankments, as a result of seasonal changes in plant transpiration and following tree felling.

Rigorous simulation of the soil-root composite requires the mechanical behaviour of the soil and roots, and the fluid (air and water) flow to be integrated and accounted for. There is considerable demand for models that can replicate triaxial, shear-box and centrifuge tests of vegetated soil [20], and account for

[1] We want to point out that different communities use different terminology to refer to soil that has both air and water in the pore space. Some use the term nonsaturated soil and others use a more accurate term of partly saturated soil. We will use the term partly saturated soil throughout this paper.

the influence of vegetation on typical engineered slopes such as railway and highway embankments [21]. A number of numerical models of vegetation effects on slopes have been developed or implemented in commercial software, but these often have limitations. For example, some approaches do not consider mechanical deformation and/or failure [22]; [17]; [23], or do not have mechanical-hydraulic coupling [24]; while other models do not account for partial saturation of the soil [25], or simplify hydraulic boundary conditions for example by ignoring rooting depth [23].

A useful model of rooted soil may need to: (i) incorporate mechanical ground movements and failure, and be able to deal with relatively large (finite) strains; (ii) couple this to partly saturated water and air flow; and (iii) represent key mechanical and hydrological aspects of the plant roots and overall plant physiology relevant for plant transpiration. This paper describes the development of a coupled physically-based soil deformation model that accounts for the influence of plant roots and is parameterised by independently measurable quantities. The aim of this paper is to show the development of this model, explaining how the root mechanical stress-strain behaviour can be incorporated, and examining the key assumptions required. Particular consideration is given to examining whether a finite-strain approach is necessary (as opposed to a typical infinitesimal engineering strain approximation); the choice of constitutive model for estimating soil deformation under root-water uptake; whether the fluids need to be treated as a two-phase, i.e. air and water, flow system; and whether deformation could be sufficient to modify the intrinsic permeability hence affect soil water flow. The individual constitutive relationships (including the soil behavioural model) can be readily changed to suit a particular scenario. Standard and relatively simple components have been adopted, so the focus is on the dynamics of coupling rather than a critique of the components, each of which is already widely accepted individually.

The basis for the modelling assumptions is set out below, with reference to the literature, and is then appraised though the investigation of simple soil-water interaction scenarios.

2 Consideration of mechanical and fluid behaviour of rooted soil

The behaviour of the soil matrix is simulated using a Modified Cam Clay model [26]; [27] with non-linear elasticity, hardening/softening, state dependency and a critical state. This well-established model is chosen because it is computationally efficient and requires only a limited number of input parameters, compared with other models simulating similar aspects of behaviour.

There is an increasing body of evidence for the nature of the mechanical behaviour of roots in soil (*e.g.* [9]; [28]; [15]). A common method for representing the action of the roots is to adjust the "apparent cohesion" parameter on a Mohr-Coulomb failure envelope [29]; [14]; [1]; [11]; [30]; [2]; [4]. This increase in "apparent cohesion" is generally estimated using the volume fraction (root area ratio) of roots and their tensile strength [31]. Fibre-bundle models are often used because in an element of soil containing roots of different diameters, roots may fail progressively rather than simultaneously [32]; [33]. To account for non-negligible bending stiffness (e.g. large diameter tree roots), [34] used a beam-on-a-non-linear-Winkler-foundation model to estimate an appropriate equivalent apparent cohesion. A different approach was followed by [3],[[35]], who simulated the hardening effect of roots empirically by means of strain-driven expansion of the pre-consolidation pressure within a Modified Cam Clay model. In essence, these approaches try to capture the behaviour of a composite (soil and root) into a single material model. The approach adopted here is different, in that the soil and roots are treated as separate phases, each with their own constitutive behaviour and both contributing to the stress state within the composite material. Thus, the parameters and history of each material may be physically characterised individually. This approach has been adopted in modelling soil reinforced by short fibres [36]; [37]. In such models, the development of root tension during strain results in an increase in the effective stress within soil around the roots, thereby increasing the shear resistance of the soil.

The root contribution is determined from knowledge of the geometry, orientation and biomechanical properties of *in-situ* root bundles via a fibre-based root-soil interaction approach [38]. This paper

describes how this phase is incorporated within the model, and illustrates it by means of a simple example.

It is assumed that air and water movement in the soil can be described by two-phase Darcy-Richards' equation. Root water uptake (RWU) may be calculated on the basis of the geometry of the root system (*e.g.* [39]; [40]; [41]; [21]; [42]; [43]; [44]; [45]; [46], which can increasingly be identified using 3D X-ray Computed Tomography (CT) scanners [47]. However, for slope-scale application it is likely that root water uptake will need to be considered macroscopically at the level of the whole planted soil [48, 49] as considering each individual root on this scale is computationally prohibitively expensive and it is unlikely each and individual root matters; rather it is their collective hydro-mechanical behaviour that matters.

RWU is frequently used as a continuum sink term with Richards' equation [50]. It is commonly taken to be proportional to the suction produced by the roots and distributed over the depth profile according to the density of roots (as parameterised by the length of roots per unit volume of soil [2]; [51]). These semi-empirical approaches typically adopt an inhibition term with increasing water suction in the soil (*e.g.* [52]; [3]; [1]; [53]; [54]). Despite its practical application, this approach has been criticised as unrepresentative of the actual process and it can be difficult to measure the parameters directly [55]. In addition, most of these models do not account for the overall plant transpiration stream from soil to roots to stems and leaves.

To account for the local pore pressure distribution around each root, researchers [49] used semi-analytical solutions (a method subsequently adopted by [56]). In [57] researchers used a localised Richards equation for the near-root flow coupled to a macroscopic water flow model. This is appropriate where roots are sparse, but [58] demonstrated that the hydraulic equilibration times are likely to be considerably shorter than other key timescales of interest such as typical growth time-scales, and environmental changes over weeks or longer. Thus, it is considered that the pressure between root sub-branches will relatively quickly reach a quasi-equilibrium value provided the root density is not too low.

Radial water flow to the root has previously been examined with reference to the detailed anatomy of the root (*e.g.* [59]; [60]; [61]; [62]). Water must pass through the cellular structure of the root cortex to reach the xylem (water-carrying capillaries). The cortex is a complex structure, but flow has been categorised into (i) apoplasmic, pressure-driven flow in the extracellular space, and (ii) symplasmic, an osmotic flow passing though cells and cell walls. In this study the bulk macroscopic water movement is taken to be dominated by the apoplasmic pathway, neglecting osmotically-driven flow [57]. However, it is relatively easy to incorporate this in our model, but in addition to the water uptake term in the Richards' equation needing to be modified, we would also need to introduce an extra equation to describe the chemical changes in the soil and within the plant. We consider this beyond the scope of this paper and refer an interested reader to the literature that deals with this [63]. The focus of this paper is to integrate the mechanical and hydrological effects plant roots have on soil.

Vertical (axial) flow inside the root xylem can be described by Poiseuille's law [64] if the distribution of the radii of functioning vessels can be estimated. However for thin roots, the axial conductivity may be considerably greater than the radial conductivity, so some studies have assumed a single constant pressure in the root system [21]; [41]; [48]. [58] showed that for maize, this may be valid for zeroth order roots (main axes), but not for first order roots (lateral branches), which could be simulated by means of a distribution coefficient on the zeroth order root, resulting in neither the radial nor the axial conductance dominating the pressure distribution in the root. Therefore, in this study, the xylem pressure is allowed to vary axially along the root.

Both the mechanical and hydraulic approaches to root behaviour will relate self-consistently to the geometric parameters of a root bundle (*i.e.* the distribution of diameters and lengths).

3 Conceptual model

Based on the considerations outlined in Section 2, an isothermal 4-phase porous system is conceptualised (Figure 1), comprising three overlapping continua: water (w), a homogeneous

granular/porous matrix (s) and air (a). The porous component is assumed to have a single set of homogeneous mechanical properties.

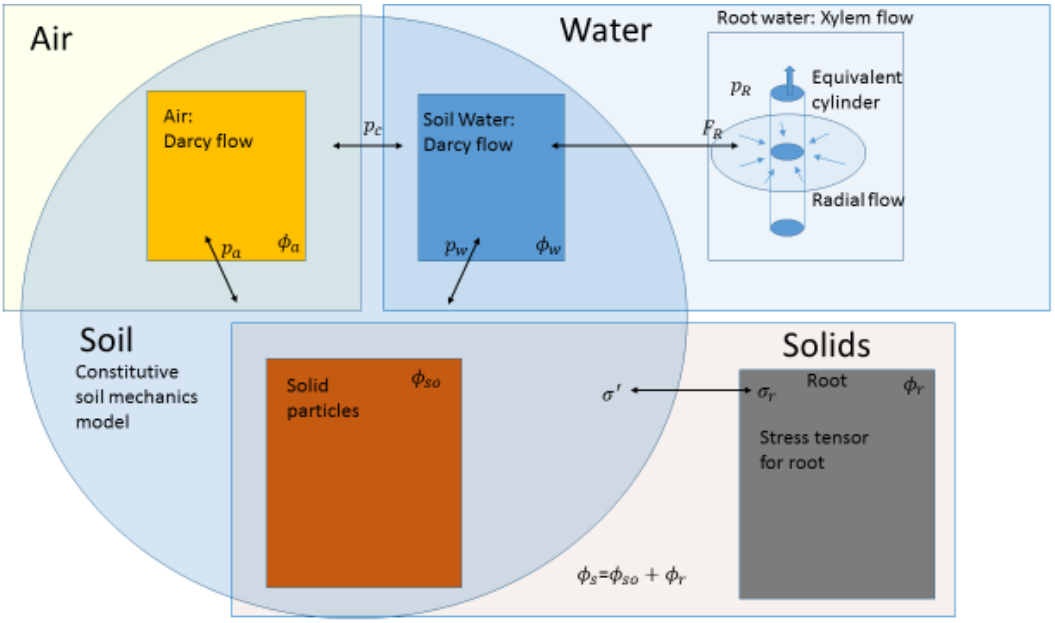

Figure 1: Schematic of multi-continuum rooted soil system. The volume is divided into four phases (*i.e.* ϕ_w, ϕ_a, ϕ_{so}, ϕ_r). The water phase has overlapping continua for flow in the soil and flow within the xylem in the root, interacting via root water uptake (F_R). The soil volume fraction comprises the solid particles, air and water phases (*i.e.* ϕ_w+ϕ_a+ϕ_{so}), but not the roots. Mechanical coupling is via the effective stress ($\boldsymbol{\sigma}'$), root stress ($\boldsymbol{\sigma_r}$) and pressure terms (p_w, p_a for water and air respectively). A capillary pressure difference (p_c) exists between the water and air phases.

The roots are envisaged as a further overlapping continuum, affecting both hydraulic and mechanical behaviours. Hydraulic interaction between the roots and the soil is via the source/sink term in the soil water equation. Mechanical interaction is via a root stress tensor, which modifies the soil effective stresses. The solid phase is coupled to the hydraulics via the effective stress. The volume taken up by plant roots is here considered as a homogenised part of the solid (*i.e.* for simplicity a soil-root composite is assumed). It would be straightforward in future studies to further partition the volume to include the root fraction explicitly.

The assumption of a bulk mechanical response relies on the averaging scale significantly exceeding the scale of inhomogeneity produced by each root. Thus the approach would not be valid for individual roots having a significant individual effect, for example a single long, thin root transmitting tensile force over a distance or a small number of large-diameter roots capable of carrying significant bending stress. The homogeneity assumption also neglects macropores, formed for example by cracking or biological

activity. Infrastructure slopes in the UK are often fairly uniformly vegetated; however, caution should be exercised, particularly for individual large plants or trees, which may possibly need to be modelled explicitly (*e.g.* [65]), and in cases where root systems are very sparse.

The compressibility of water and of the solid particles is assumed to be negligible. Owing to the high diffusivity of air, gas compressibility is only important under special circumstances (for example compression of individual entrapped air bubbles beneath a saturated wetting front); hence, following [66], it is neglected in this paper.

The difference in pressure between the two fluid phases is described by a single capillary pressure curve. For simplicity in introducing the model, wetting and drying hysteresis effects, and coupling between void ratio and moisture retention [67], are neglected. As data and necessity dictate, such constitutive relationships could be easily be incorporated if needed. The possibility of mixed phases or isolated (static, non-percolating) phases is also neglected.

A finite (i.e. large or non-infinitesimal) strain approach is adopted, since it does not require the assumption of infinitesimal engineering strain. Thus the model is not restricted to small strain applications, allowing it to be used in conditions where significant deformation occurs e.g. shear box tests and extensively plastically-deformed slopes. Furthermore, roots typically require large strains to mobilise their full capacity (15-20% typically). Therefore, to investigate the behaviour of rooted soil at peak root capacity, soil behaviour may have to be cast in a large-deformation framework to remain accurate.

The concept of combined modelling presented in this paper is novel in that it integrates a large-strain mechanical model of soil coupled with partly saturated air and water flow and physically-based root water uptake equations. This moves away from more empirical approaches for root water uptake (*e.g.* [52]), for which the parameters are not as easily obtainable by direct measurement.

4 Model development

The kinematic behaviour of a solid continuum at large strains requires rigorous treatment [68]; [69]; [70]). Within the Eulerian (spatial) reference frame, a point in space is described by vector $\boldsymbol{x}$ and within the Lagrangian (material) reference frame, a point in the material by $\boldsymbol{X}$. Displacement of the material in relation to the reference frame is $\boldsymbol{u} = \boldsymbol{x} - \boldsymbol{X}$. The displacement vectors can be decomposed into $= x\hat{\boldsymbol{\imath}} + y\hat{\boldsymbol{\jmath}} + z\hat{\boldsymbol{k}}$ and $= X\hat{\boldsymbol{\imath}} + Y\hat{\boldsymbol{\jmath}} + Z\hat{\boldsymbol{k}}$, where $\hat{\boldsymbol{\imath}}$ and $\hat{\boldsymbol{\jmath}}$ are unit vectors on the horizontal plane and $\hat{\boldsymbol{k}}$ is the upward vertical unit normal.

The governing equations are cast in Eulerian co-ordinates, in which physical parameters are readily interpreted. However, the domain itself changes size and shape and the boundaries move, which needs careful numerical treatment. For numerical implementation, the model is therefore converted to Lagrangian co-ordinates, where nominal parameters referenced to the initial reference state and boundaries are fixed (as detailed in Supplementary Material A).

4.1 Eulerian equations

As shown in Figure 1, the total volume is divided into four distinct phases of air (a), root (r), soil (s) and water (w). The volume fractions, ϕ, of each phase sum to unity, *i.e.*:

$$\phi_w + \phi_{so} + \phi_r + \phi_a = 1, \qquad [1]$$

The solid volume fraction $\phi_s(x,t)$ is the sum of the soil and root components, *i.e.* $\phi_s = \phi_{so} + \phi_r$ and is related to the initial solid fraction, $\phi_{s,0} = \phi_s(x,0)$ via the Jacobian determinant $J = \det(\boldsymbol{F})$, *i.e.*:

$$\phi_s = \frac{\phi_{so}}{J}, \qquad [2]$$

where the deformation-gradient tensor, $\boldsymbol{F}$, defined in relation to the Eulerian frame [70], is:

$$\boldsymbol{F}_{ij}^{-1} = I - \frac{\partial \boldsymbol{u_i}}{\partial \boldsymbol{x_j}}. \qquad [3]$$

The solid velocity can also be derived in relation to $\boldsymbol{x}$:

$$\boldsymbol{v_s} = (I - \nabla \boldsymbol{u})^{-1} . \left.\frac{\partial \boldsymbol{u}}{\partial t}\right|_{\boldsymbol{x}} = \boldsymbol{F} . \left.\frac{\partial \boldsymbol{u}}{\partial t}\right|_{\boldsymbol{x}}. \qquad [4]$$

The mass (volume) balance of the water phase is given by:

$$\frac{\partial \phi_w}{\partial t} + \nabla.(\phi_w \boldsymbol{v_w}) = -F_R, \quad [5]$$

where $F_R(\boldsymbol{x}, t)$ is a water-sink term representing root water uptake (RWU). The mass conservation equation for the air phase is:

$$\frac{\partial \phi_a}{\partial t} + \nabla.(\phi_a \boldsymbol{v_a}) = 0, \quad [6]$$

where gaseous exchange between the roots and the soil is neglected. Equation [5] enables Darcy's law to be implemented for water flow relative to the soil, *i.e.* $\phi_w(\boldsymbol{v_w} - \boldsymbol{v_s}) = -(k/\mu)\left(\nabla p_w + \rho g \widehat{\boldsymbol{k}}\right)$, within the water balance:

$$\frac{\partial \phi_w}{\partial t} + \nabla.\left[-\frac{k}{\mu}\left(\nabla p_w + \rho g \widehat{\boldsymbol{k}}\right)\right] + \nabla.(\phi_w \boldsymbol{v_s}) = -F_R. \quad [7]$$

where p_w is soil pore water pressure, ρ is water density, g is gravitational acceleration, k is the Darcy permeability of the soil to water and μ is the water (dynamic) viscosity. Similarly, manipulating Equation [6] enables implementation of Darcy's law for air flow relative to the solid, *i.e.* $\phi_a(\boldsymbol{v}_a - \boldsymbol{v_s}) = -(k/\mu)\left(\nabla p_a + \rho_a g \widehat{\boldsymbol{k}}\right)$, within the air balance:

$$\frac{\partial \phi_a}{\partial t} + \nabla.\left[-\frac{k_a}{\mu_a}\left(\nabla p_a + \rho_a g \widehat{\boldsymbol{k}}\right)\right] + \nabla.[\boldsymbol{v_s}\phi_a] = 0, \quad [8]$$

where p_a is the air pressure, k_a the Darcy permeability of the soil to air, ρ_a the air density and μ_a the air (dynamic) viscosity. Additionally, a van Genuchten [71] water-retention relationship is assumed, in which the water saturation, defined as $S_w = \frac{\phi_w}{1-\phi_s}$, is a function of the air and water pressures:

$$S_w = \frac{1}{\left[1+\left(\frac{\alpha(p_a - p_w)}{\rho g}\right)^N\right]^M}, \text{ for } p_a > p_w \text{ , else } S_w = 1, \quad [9]$$

where N is an exponent, $M = 1 - \frac{1}{N}$, α is a soil-water retention parameter. More generally, the moisture retention relationship observed in experiments has a separate wetting / drying path (i.e. exhibits hysteresis). It is also altered by changes to the distribution of pore sizes and shapes, which may be brought about by both roots occupying pore space, organic matter content changes and deformations to the solid skeleton [67]. In principle, equation [9] can be modified to reflect these effects, where

sufficient data are available for the soil; however this is neglected here to retain the simplest possible treatment.

In partly saturated conditions, a proportion of the pore space becomes unavailable for water flow. This is addressed by introducing an effective permeability for water flow, k_w, which, following [71], depends on the relative saturation ratio S_w as:

$$k_w = k\, S_w^L \left[1 - \left(1 - S_w^{\frac{1}{M}}\right)^M\right]^2 \text{, for } p_a > p_w \text{, else } k = k_s, \qquad [10]$$

where k is the intrinsic permeability, and L and M are constants. Similarly, the effective permeability for air, k_a, is given by [72]:

$$k_a = k(1 - S_w)^L \left[1 - S_w^{\frac{1}{M}}\right]^{2M} \text{, for } p_a > p_w \text{ , else } k_a = 0. \quad [11]$$

The model includes a further level of coupling, whereby the initial intrinsic permeability k_0 may vary with the void space geometry [73] according to a Kozeny-Carman type relationship [70];

$$k = k_0 \frac{\left(1-\phi_{f0}\right)^2}{\phi_{f0}^3} \frac{\phi_f^3}{\left(1-\phi_f\right)^2}, \qquad [12]$$

where k_0 is the intrinsic permeability at a reference stress of 4 kPa, the total (fluid, i.e. air and water filled) porosity is $\phi_f = \phi_w + \phi_a$ and the subscripts 0 denote initial conditions. Refuting earlier assertions that this relationship does not apply to very fine-grained materials, [74] show that, once artefacts and experimental error are eliminated, the equation predicts the saturated hydraulic conductivity of most soils fairly well.

A simple upscaled approach for water pressure in an equivalent single root is adopted. This is a first-order RWU relationship for steady state radial pressure-driven flow [75]:

$$F_R(z,t) = \pi d_r k_R l_d (p_w - p_R), \qquad [13]$$

where d_r is the root diameter, k_R is the root radial conductivity (m/Pa/s) (a bulk measure of the cross-sectional geometry and effective diffusivity over the ensemble of roots) and p_R is the root internal xylem

pressure. This is a quasi-steady state simplification of unsteady pressure transmission through the anatomy of the root [59]. [58] showed that, since the cortex dimension scales with the size of the root, $\pi d_r k_R$ may be considered to be independent of root diameter and therefore potentially applicable to a range of root sizes. In general k_R is a function of the distance down the root, but it is held constant for the purposes of this paper, aggregating all depth dependence in the root transfer term into l_d, which is the length of roots in each unit volume of soil. Treating any changes to internal water storage as negligible, the root pressure along a non-branching vertical root is given by:

$$\pi d_r k_R (p_w - p_R) = -\frac{\partial}{\partial z}\left[k_z\left(\frac{\partial p_R}{\partial z} + \rho g\right)\right], \quad [14]$$

where k_z is the root axial conductivity (m^4/Pa/s). Assuming k_z to be constant with depth gives:

$$\pi d_r k_R (p_w - p_R) = -k_z \frac{\partial^2 p_R}{\partial z^2}. \quad [15]$$

Since xylem capillary flow may be reasonably estimated using Poiseuille flow, the bulk rate is given as the summation of all individual xylem vessel contributions [58]:

$$k_z = \sum_i \frac{\pi n_i R_i^4}{8\mu}, \quad [16]$$

where R_i is the radius of the xylem vessel, n_i is the number of open xylem vessels with cross-sectional radius R_i and i is the index of each radius category. k_z may therefore be either measured [64] or estimated based on the xylem radius distribution using equation [16]. This single cylindrical equivalent root model can be used to aggregate the RWU from higher order lateral roots by assuming the flow rate from higher order roots to be smoothly distributed over the zeroth order roots [58]. The upper bound for RWU occurs when the soil water is at atmospheric pressure and the root base suction pressure is a maximum. The plant root to stem to leaves transpiration stream is captured as a boundary condition to equation [15] as it links leaf water potential to the atmospheric pressure and ultimately appears as a boundary condition at the base of the root system for equation [15].

The final component of the model is the mechanical behaviour of the solid skeleton. Neglecting inertial effects, the equation for force equilibrium in Eulerian co-ordinates is:

$$\boldsymbol{f_v} + \nabla.\boldsymbol{\sigma} = 0, \qquad [17]$$

where compressional stress is defined as positive on the inward normal, the (Cauchy) stress tensor is denoted by $\boldsymbol{\sigma}$ and the gravity body force per unit volume, $\boldsymbol{f_v} = -g(\rho_{so}\phi_{so} + \rho_w\phi_w + \rho_a\phi_a + \rho_r\phi_r)\widehat{\boldsymbol{k}}$. Expressing the force balance in terms of the effective stress, $\boldsymbol{\sigma}'$, gives:

$$\nabla.\boldsymbol{\sigma} = \nabla.\{(1-\phi_r)[\boldsymbol{\sigma}' + p_a I - \chi(p_a - p_w)I] + \phi_r\boldsymbol{\sigma_r}\} = -\boldsymbol{f_v}. \qquad [18]$$

where I is the identity matrix. Coupling of the solid mechanics with the fluid pressures thus arises via the effective stress. Here, he effective soil stress is represented by the so-called Bishop stress, $\boldsymbol{\sigma}_i' = (\boldsymbol{\sigma} - p_a) + \chi(p_a - p_w)$, with the parameter $\chi = S_w^{\beta}$ [76] where β is an exponent that varies as a function of plasticity index, after [77]. It is known that $\boldsymbol{\sigma}_i'$ does not represent a true effective stress for soils below a certain critical initial degree of saturation (which may be as high as 90 % for clays), as it does not account for the volumetric compression or collapse that can occur on wetting. However, it is shown by [78] that the Bishop stress expression with χ replaced by the saturation ratio S_w does have physical significance. In any case, this simplification can be revised if data show χ to be a non-linear function of S_w at high and low water contents [79]; [80]). $\boldsymbol{\sigma_r}$ is the (Cauchy) stress tensor within the root volume fraction. Roots can develop tension as they are extended, and thicker roots may hold shear and bending stress. A key facet of the model is the assumption that the constitutive behaviour of the soil is unaffected by the presence of the roots, other than through modification of the effective stress tensor. In essence, the soil is treated as a fallow material, with the roots influencing its behaviour through modification of the effective stress state.

The constitutive relationship between effective stress and strain for the soil can be computed in terms of elastic behaviour as $\boldsymbol{\sigma}' = \boldsymbol{C}:\boldsymbol{\varepsilon_e}$, where $\boldsymbol{C}$ is the (fourth-order) elastic tensor. An appropriate elastic strain measure is the Euler-Almansi strain, defined by:

$$\boldsymbol{\varepsilon_e} = \frac{1}{2}(I - \boldsymbol{F_e^{-T}F_e^{-1}}), \qquad [19]$$

where the elastic deformation gradient (Eq. 3) is given by $\boldsymbol{F_e} = \boldsymbol{F}\boldsymbol{F_p^{-1}}$ and $\boldsymbol{F_p}$ is the plastic deformation gradient tensor. Rearranging Equation [18] gives:

$$\nabla.\boldsymbol{\sigma} = \nabla.\{(1-\phi_r)[\boldsymbol{C}:\boldsymbol{\varepsilon_e} + p_w S_w I + p_a(1-S_w)I] + \phi_r \boldsymbol{\sigma_r}\} = -\boldsymbol{f_v}, \qquad [20]$$

For simplicity, residual saturations of air and water are assumed to be zero.

The Modified Cam-Clay (MCC) model [26]; [27] is used to populate the elasticity tensor C, with stress-dependent stiffnesses. The elastic response (within the yield surface) is expressed succinctly using a decomposition into volumetric and deviatoric components [27], as:

$$\begin{bmatrix}\delta\varepsilon_V^e \\ \delta\varepsilon_q^e\end{bmatrix} = \begin{bmatrix}\kappa/vp' & 0 \\ 0 & 1/3G\end{bmatrix}\begin{bmatrix}\delta p' \\ \delta q\end{bmatrix}, \qquad [21]$$

where ε_V^e is the elastic volumetric strain, ε_q^e is the elastic deviatoric strain, $p' = \frac{1}{3}tr(\boldsymbol{\sigma}')$ is the mean effective stress, q is the deviator (von Mises) stress and κ is the slope of the elastic (unload-reload) line in the v:lnp' plane. There is a choice as to whether to fix the shear modulus G or the Poisson's ratio υ [27]; υ is fixed here, hence the shear modulus is calculated as:

$$G = \frac{3(1-2\upsilon)vp\prime}{2\kappa(1+\upsilon)}. \qquad [22]$$

The elliptical yield surface is given by:

$$f = q^2 - M^2\left[p'\left(p'_{pc} - p'\right)\right] = 0, \qquad [23]$$

where M is the slope of the critical state line in the q:p' plane. It is assumed that the soil obeys the normality condition, *i.e.* that the vector for plastic strain increments is in the direction of the outward normal to the yield envelope. The plastic response is given as:

$$\begin{bmatrix}\delta\varepsilon_V^p \\ \delta\varepsilon_q^p\end{bmatrix} = \frac{(\lambda-\kappa)}{vp\prime(M^2+\eta^2)}\begin{bmatrix}(M^2-\eta^2) & 2\eta \\ 2\eta & 4\eta^2/(M^2-\eta^2)\end{bmatrix}\begin{bmatrix}\delta p' \\ \delta q\end{bmatrix}, \qquad [24]$$

where $\eta = q/p'$ and λ and κ are the slopes (in the v:lnp' plane) of the normal compression line and unload-reload lines, respectively.

The constitutive relationship, $\boldsymbol{C_r}$, between the root stress and root strain can be formulated based on upscaled root data (including the distribution of root orientation, thickness and breaking strain, consideration of soil-root friction and inclusion of root failure mechanisms). A detailed methodology for this process is given by Meijer et al. (2020), in relation to new mechanical test data.

For the purposes here of demonstrating the mechanical coupling under 1D loading conditions, a very simple root model is assumed as follows: there is a rigid root-soil interface (i.e. the root strains are equal to the soil strains, $\boldsymbol{\varepsilon_r} = \boldsymbol{\varepsilon}$); the roots provide only a vertical tensional force; root stress occurs only in tension; the roots act after time t_r, otherwise hold no tension; the cross-sectional area of the roots is unchanged by stretching (i.e. Poisson's ratio for the roots is zero); there is a linear relationship between tensional stress and strain, cast in an intermediate reference frame that defines the initial state of the roots; see Supplementary Information A; and the roots do not reach their breaking strain.

The complete model thus comprises 6 independent equations for 6 independent variables (p, p_a, p_R ,u_x, u_y, u_z), which are solved together with initial and boundary conditions on the external surface, $\boldsymbol{\Gamma}$. The equations are summarised in Table S1 in Supplementary Material A. Initial and boundary conditions for a particular scenario are given in Section 5.1. The proportions of each phase are calculated as $\phi_s = \phi_{s0}/J$, $\phi_w = S_w(1-\phi_s)$ and $\phi_a = 1 - \phi_w - \phi_s$. The model is implemented as a system of partial differential equations (PDEs) using COMSOL 5.3a (2016) [81], via the inbuilt 'general form PDE'. The COMSOL Structural Mechanics and Geomechanics modules were used to solve the equations of the mechanics of the deforming solid and for the COMSOL implementation of Modified Cam Clay. Simulations to verify the approach are given in Supplementary Material B.

5 Simulation

5.1 Model set-up

5.1.1 Boundary and Initial Conditions

The model is used to examine finite elasto-plastic deformation of a vegetated soil during a drying-wetting cycle. The soil is first consolidated under self-weight (for 10 days), dried for 120 days by root water uptake (RWU) and downward drainage, and then re-wetted by continuous rainfall. Three variants of this scenario are simulated. In **Simulation 1** the air pressure is kept constant at atmospheric pressure and the intrinsic permeability is assumed to be constant. **Simulation 2** is identical to Simulation 1, except that the intrinsic permeability of the soil is varied to account for void contraction. **Simulation 3** is also

identical to Simulation 1, except that the air pressure is computed. In Simulations 1 and 2, the air phase pressure – which should be governed by equation [8] – is held constant at $p_a = p_{atm}$; a typical simplification applied to partly saturated soils. In **Simulation 4**, the root stress provides a tensional stress proportional to the extension experienced during the re-wetting phase.

The soil is bounded by vertical boundaries allowing frictionless vertical movement, but preventing lateral movement (analogous to an idealised oedometer or a one-dimensional (1D) soil column). Thus the soil solid undergoes 1D consolidation and subsequent swelling, driven by its weight and changes in effective stress due to changing pore water pressures. The consolidation under self-weight is a modelling necessity and is not intended to represent a real geological process, although the ramping of the self-weight load has similarity with "spin-up" in a geotechnical centrifuge.

The soil profile is initially 5 m deep with the upper surface flat. The upper boundary is defined as the free surface, $\boldsymbol{x} \in \boldsymbol{\Gamma}(\boldsymbol{x}, t)$, and moves as the solid deforms, *i.e.* as $\boldsymbol{\Gamma} = \boldsymbol{\Gamma_0} + \boldsymbol{u}$, where the initial surface $\boldsymbol{\Gamma_0}$ is a horizontal plane at elevation $z = D$ above the base. On the upper boundary, the column has a water flux boundary condition for the infiltration of rainfall, R, which is set to 0 for the first 130 days and to 5 mm/d thereafter. For air, the upper boundary is given by the fixed atmospheric pressure condition, $p_a = p_{atm}$. The lower boundary is restrained from moving in all degrees of freedom. At the base ($z = 0$) the water pressure is fixed to $p_w = p_{atm}$, ensuring that the lower boundary is always saturated with water, making it impermeable to air and allowing drainage from the base. The root base pressure (i.e., the pressure within the root at its base, at the soil surface) P = -1 MPa during root water uptake (from 10 to 130 days) and is otherwise 0 MPa. Root base pressure P integrates all above ground plant transpiration effects into one single parameter accounting for the atmospheric temperature, pressure, humidity, windspeed etc. outside of the plant and the plant above ground stem and leaf stomatal conductance all of which can and do vary with time owing to the interaction between vegetation and the weather [82], [83]. But for illustration purposes we assume it to be constant during the day and zero during the night.

There is a no-flow condition at the tip of the root (initially located at a distance L_R below the base of the root), as owing to root physiology roots do not take up or bleed water through their tips. The initial condition for the whole solid is a displacement of zero, $\boldsymbol{u} = 0$. The initial condition for the pore water pressure is for the soil to be just less than fully saturated, *i.e.*, $p = p_{atm} - 1$ kPa. The initial xylem pressure p_R is in equilibrium with the initial local pore water pressure, *i.e.*, $p_R = p$. Prior to root water uptake, the soil is consolidated under self-weight, with the body force increased linearly over 10 days starting from zero.

5.1.2 Parameters

The parameters used in the simulations, based broadly on a clayey silty sand known as Bullionfield soil [12], are given in Table 1. As in conventional soil mechanics practice, it is assumed that the soil grains are incompressible.

Table 1: Simulation parameters

Parameter	Definition	Value
	Fluid properties	
k	Intrinsic permeability of soil	$k_s = k_{s0}$ =1×10^{-13} m^2 (equivalent to a hydraulic conductivity of water K_s~1×10^{-6} m/s) (except in simulation 2, where k_s is calculated using equation [12])
μ	Viscosity of water	0.001 Pa.s
ρ	Density of water	1000 kg/m^3
μ_a	Viscosity of air	1.81×10^{-5} Pa.s
ρ_a	Density of air	1.2 kg/m^3
p_a	Air pressure	p_{atm} (except in simulation 3, when $p_a$is calculated using equation [8])
	Water retention	
α	Retention parameter	1.5 1/m
N	Retention parameter	1.43
L	Permeability parameter	0.5
ϕ_{s0}	Initial solid volume fraction	0.5 (corresponding to e_0 = 1 at the reference pressure of 4 kPa)
	Rainfall and root water uptake	
R	Rainfall rate	5 mm/d for t>130 days (otherwise 0 mm/d)
L_R	Depth of root zone	1 m
P	Root base suction pressure	-1 MPa for 10<t<130 days (otherwise 0 MPa)
k_R	Root radial conductivity	1×10^{-14} m/s/Pa for t<130 days (otherwise 0 m/s/Pa)
k_z	Root axial conductivity	1×10^{-13} m^4/s/Pa
l_{d0}	Root length per soil volume density	1785 m/m^3 [83]
d_r	Root diameter	0.001 m [58]
	Mechanical properties	

Parameter	Definition	Value
β	Effective stress exponent	1
ν	Poisson's ratio	0.4
κ	Elastic Stiffness gradient (unload / reload line in the v:lnp' plane) for MCC	0.015
λ	Gradient of normal compression line in the v:lnp' plane for MCC	0.1
M	Slope of critical-state line in the q:p' plane for MCC	1.35
p_0	Reference (and initial) pressure for MCC	4 kPa
p'_{pc0}	Pre-Consolidation pressure for MCC	50 kPa
e_0	Void ratio at initial (reference) pressure for MCC	1 (corresponding to ϕ_{s0} = 0.5)
ρ_s	Density of solid grains	2650 kg/m^3
σ_r, ϕ_r	Root stress tensor and volume fractions	Zero For simulation 4, $\sigma_r$is computed and ϕ_{r0}=0.01
E_r	Elastic modulus of root	100 MPa during extensional phase for Simulation 4. Otherwise 0. Broadly representative of woody roots (Sitka spruce and blackcurrant) [84]; young willow and gorse, and fibrous roots (festulolium grass) [12]
Model geometry		
L_R	Root length	1 m
D	Domain height	5 m

A wide variety of values for the root uptake parameters k_R and k_z have previously been identified, depending on species [85]; [64]; [21]. $k_z = 1\times10^{-13}$ m^4/s/Pa is adopted here as central to the range reported in the literature. k_R is set to 1×10^{-14} m/s/Pa, which gives a maximum root water uptake of 4.8 mm/d when p_R = 1 MPa and p_w = 0 MPa (this is based on observations at Newbury, UK, by [86] and gives a July monthly average potential evapotranspiration of between 2 and 3 mm/d). For the period of zero RWU, k_R is set to 0 m/s/Pa for t>130 days.

In Simulations 1-3, all terms in the root stress tensor $\boldsymbol{\sigma_r}$ and the volume fraction allocated to the roots ϕ_r are zero. However, in Simulation 4, the root stress tensor is computed based on the deformation that takes place after 130 days (i.e. the start of the wetting period). The root is assumed to be anchored from this point in time, with zero slip between the root and the soil. This is primarily a modelling necessity, although it is likely that by this time the root has been able to fix itself to the soil through the growth of short lateral branches.

5.2 Model results

Simulation 1: fixed pore air pressure p_a and intrinsic permeability k

Figure 2a shows the period of soil drying by RWU, followed by rain wetting. The rate of drainage from the base of the column decays over time as the lower part of the column approaches a hydrostatic equilibrium condition. The initial RWU is 4.78 mm/d, declining to 0.6 mm/d by 130 days because of the reduction in the pressure difference between the soil and the xylem as the soil pore water pressure falls as a result of RWU and drainage (the fall in pore water pressure also causes the mean effective stresses to rise). Thereafter, rainfall causes a downward-moving wetting front, which restores the pore pressures.

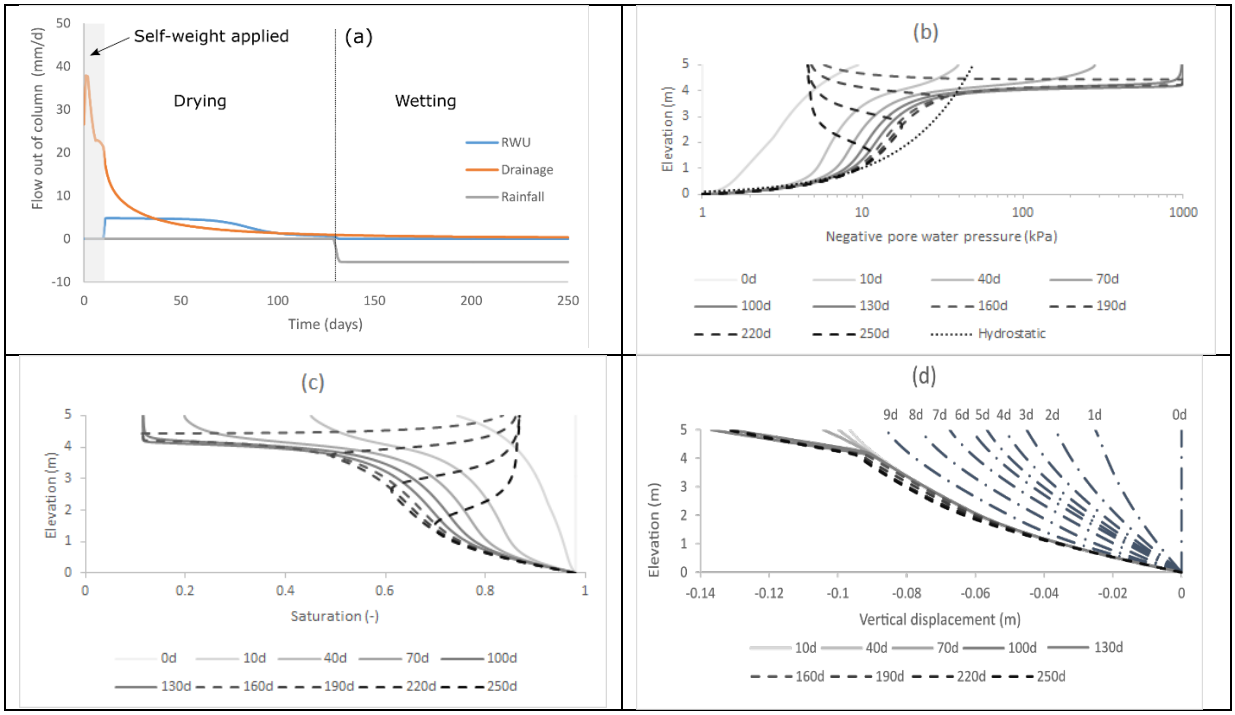

Figure 2 – simulation 1. 10 days of settlement, 120 days of drying due to RWU (solid lines), followed by 120 days of rewetting due to 5 mm rainfall (dashed lines) (a) Flows out of the column by downwards drainage, RWU and Rainfall into the column (negative outflow) (b) pore-pressure profiles with depth, (c) the corresponding degree of saturation and (d) vertical displacement. Legend gives times (in days) from the start of simulation (shade darkens with time, dashed line for wetting period, solid lines for drying period and dot-dash lines for first 10 days).

Figure 2b shows relatively modest reductions in pore water pressures after ten days of consolidation and downward drainage. RWU then generates stronger negative pore water pressures (plotted every 30 days after the initial consolidation period). By 130 days from the start of the simulation, the pore pressure in the soil adjacent to the roots (*i.e.* in the top 1 m of soil) has approached the xylem pressure of -1 MPa. Thereafter, pore water pressures recover as a wetting front moves down from the surface in response to rainfall.

The degree of saturation (Figure 2c), mapped from the pore water pressure via the soil water characteristic curve or water retention relationship (Equation [9]), follows a similar pattern. At 250 days the soil is drier than the initial state as a result of the vertical downward drainage through the base of the column. The pressures are tending towards a steady-state value of ~4.7 kPa, whereat the hydraulic conductivity is equal to the 5 mm/d rainfall rate.

Figure 2d shows how ~100 mm of vertical surface displacement accumulates progressively over the 5 m soil profile during the ten days of consolidation at the start of the simulation. Thereafter the soil dries and contracts, giving a maximum downward vertical displacement of 140 mm at the ground surface before rewetting causes upward swelling. Dewatering of soil has therefore caused ~40 mm of surface movement, which is in order of magnitude terms consistent with values typically observed on vegetated slopes [19].

The resulting stress states and volumetric compressions are shown in Figure 3 for the soil adjacent to the mid-point of the root (*i.e.* 0.5 m below the soil surface) and 0.5 m above the base of the model.

The mid-root results are shown in the left-hand column of Figure 3. Consolidation (during the application of self-weight) compresses the soil elastically. At the end of the consolidation period (10 days) the ratio of horizontal to vertical effective stress $K_0 = 0.63$. Thereafter, the soil compresses due to the lowering of the pore water pressures by RWU. The yield surface is encountered at 72 days, after which the soil compresses plastically in the vertical direction, the yield surface being pushed out to p'_{pc} = 104.9 kPa. The void ratio reduces at a gradient (with increase in the natural logarithm of the mean effective stress) of κ=0.015, steepening to λ=0.1 along the isotropic normal consolidation line during plastic deformation. On re-wetting the soil unloads elastically. At 164 days, the unloading stress path crosses the x-axis, giving zero deviatoric stress. Owing to the continued increase in pore pressure due to rainfall, the vertical effective stress then rises above the lateral effective stress (thereby increasing the deviator stress back above zero). Figure 3c shows that by the end of the simulation, the soil has contracted relative to the

initial condition (*i.e.*, the re-wetting has not returned the soil to the starting point, but to a void ratio of 0.915 compared with 1.0 initially).

The right-hand column in Figure 3 shows the behaviour deeper in the soil, which is dominated by self-weight. The soil at 0.5 m elevation encounters the yield surface after 7 days and the consolidation pressure p'_{pc} increases to 71 kPa. Thereafter, the soil undergoes a small elastic swelling. This expansion is due to the reduction in total stress at this depth, owing to the removal of water (hence reduction in soil unit weight) from the soil above by RWU. p' decreases as the roots remove water, then recovers after 130 days in response to the continuous rainfall. Thus RWU causes the soil to follow opposite loading directions at different depths, the effective stress being dominated by changes to the pore pressure at shallow depth (resulting in a large increase) and by changes in the total stress associated with a reduced unit weight of the overlying soil at greater depth (resulting in a small decrease).

For comparison, the responses given by a linear-elastic (LE) soil model are plotted in the top row of Figure 3. The LE bulk modulus is matched at the initial condition, *i.e.* $K = vp'_{ref}/\kappa$. The MCC model stiffens with increasing mean effective stress, hence diverges from the LE loading path. It is evident that neither a LE nor a monotonic non-linear model would adequately simulate elastic loading and irreversible hardening behaviour. The model indicates that the range of effective stress potentially encountered by soils in the root zone is too large for the mechanical response to be considered linear with any degree of accuracy.

The largest (Euler-Almansi) volumetric strain encountered at the half-rooting depth (0.5 m below the surface) is -4.2%. The engineering strain (based on an assumption of infinitesimal strain) is -4.0% (*i.e.* there is a 5% relative error between the strains). Given that the root system base pressure is set to -1 MPa, yet plant roots are capable of inducing soil pressures down to -1.5 MPa [9], there is potential for even greater strains generated purely by root water uptake than observed in this simulation. Hence the errors introduced by assuming small strains may be significant for some applications.

Elevation 4.5m (mid-root)	Elevation 0.5m
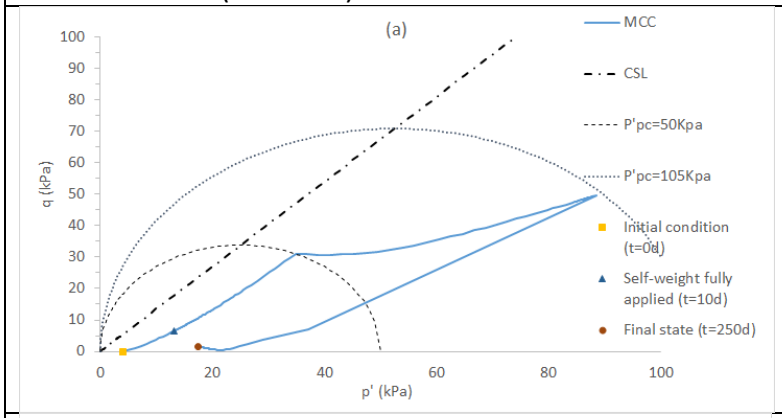	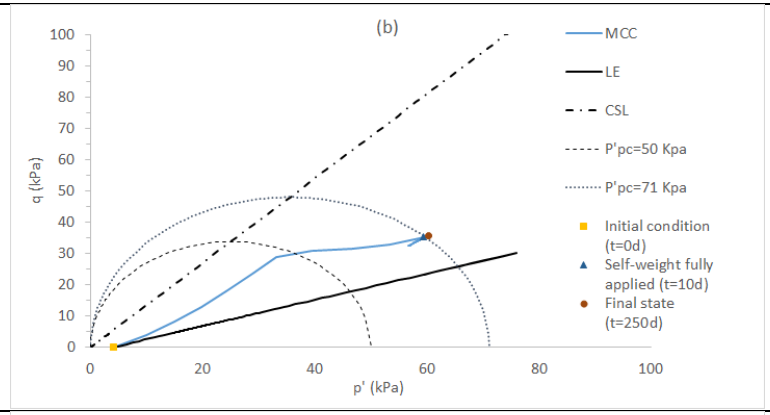
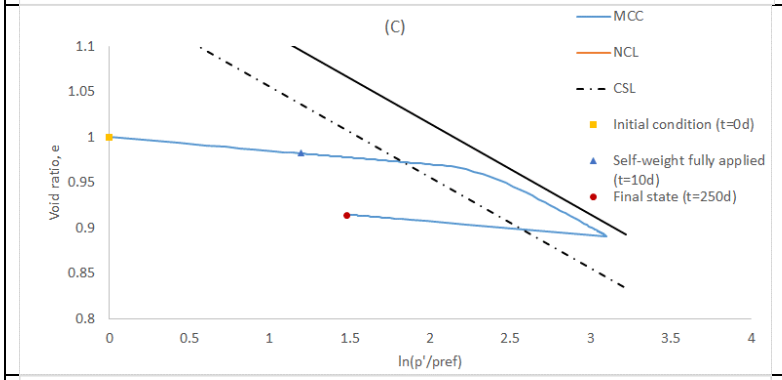	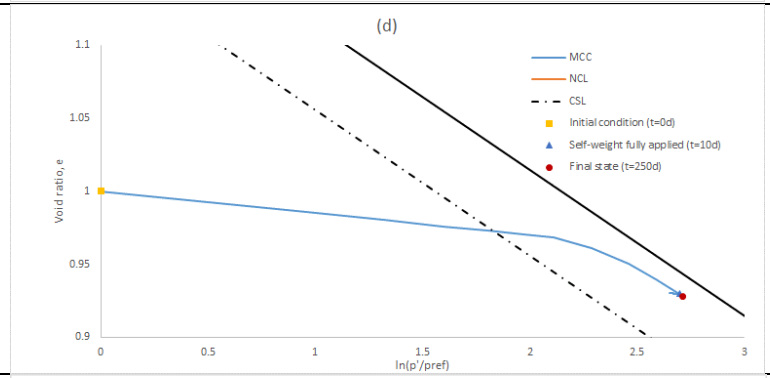
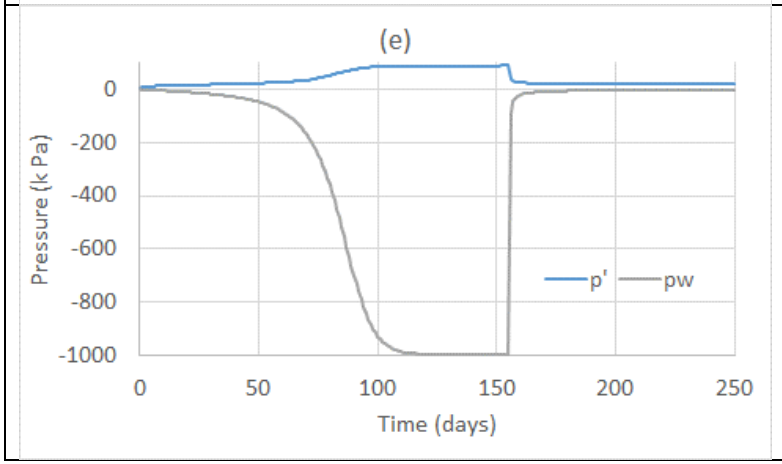	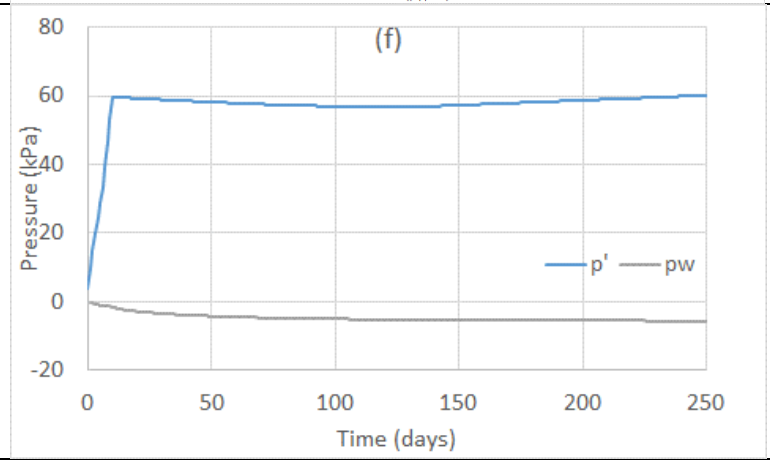

Figure 3: Simulation 1. 10 days of settlement due to self-weight, followed by 120 days of drying due to RWU, then 120 days of rewetting due to 5 mm rainfall. Left hand column is for 0.5 m below the surface (*i.e.* at 4.5 m elevation, midway down the root zone): (a) Stress path for the soil (p' is effective stress and q is deviator stress; defined in the nomenclature) (c) void ratio, where solid line is the Modified Cam-Clay model (MCC) state path and (e) effective stress p' and pore water pressure p_w against time. Right hand column is for 0.5 m elevation (*i.e.* 4.5 m from the surface): (b) stress path for the soil, (d) void ratio and (e) effective stress p' and pore water pressure p_w against time. LE denotes Linear-Elastic, CSL is the Critical State Line.

Simulation 2: variable intrinsic saturated permeability k_s

Given the potentially significant changes in effective stress due to RWU it may be possible that the deformation of the solid skeleton is sufficient to affect the permeability, hence the coupled fluid flow and mechanical response. This has been shown to affect consolidation in saturated media at large strains [87]; [70]. However, Simulation 2 showed no significant differences in pore pressures compared with those assuming a constant intrinsic permeability. Adjacent to the root, the soil pressures approached -1 MPa after 120 days and the volumetric solid fraction (ϕ_s) increased from 0.5 to 0.52. From Equation [12], the corresponding intrinsic permeability is reduced to 80% of the uncompressed value. The reduction in k due to desaturation calculated by Equation [10] is eight orders of magnitudes greater (to $k = 8\times10^{-21}\text{m}^2$); it is this that dominates water flow, hence pore pressures and displacements. Thus given the assumptions made and for the conditions simulated, the degree of saturation (*i.e.* Equation [10]) dominates the hydraulic conductivity – any changes arising from changes in porosity are very much a second order effect. It is possible, however, that if a sufficient surcharge is applied to a soil close to saturation, changes in k due to changes in porosity may become significant. This might be important, for example during spin-up in a geotechnical centrifuge (*e.g.* Liang *et al*., 2017).

Simulation 3: dynamic air phase (variable pore air pressure p_a)

The air-phase pressure is not kept constant in this simulation, but is calculated using Equation 8. The lower boundary is impermeable to air (i.e., a zero-flux condition applies) and the upper boundary is set to atmospheric pressure. The initial air pressure condition is a positive aerostatic distribution, *i.e.* $p_a = \rho_a g(D - z)$, giving a positive air pressure of 0.06 kPa at the base of the model.

Downward drainage of water by gravity followed by RWU starting at day 10 causes air to move into the soil, under a relative suction, to replace some of the volume of water drained. Conversely, when rainfall is wetting the soil, the internal air pressure rises above the aerostatic line and air is discharged from the surface of the soil. The soil conductivity for air is higher than for water, and the pressure gradient for a given volumetric flow rate is proportionately lower. The air pressure at the base of the model reaches a maximum at the end of the simulation of 0.21 kPa. This is negligible in comparison with the changes in pore water pressure, which were up to 1 MPa. For simulations under such circumstances, it may be expedient (to save on computational time) to fix the air pressure, as is frequently done in standard unsaturated zone water flow simulations.

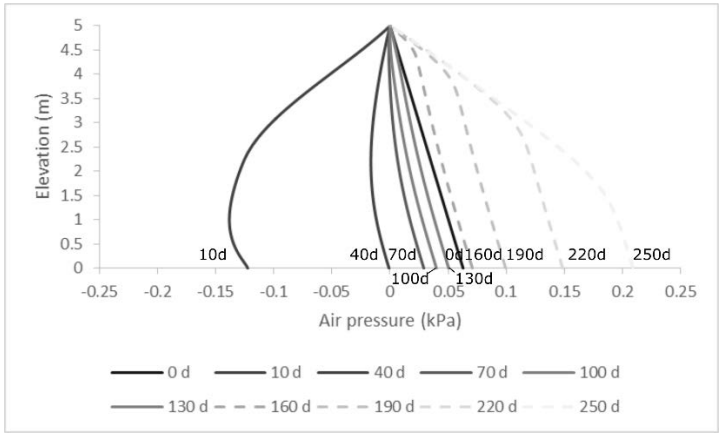

Figure 4: Pore air pressure for Simulation 3. 10 days of settlement, 120 days (d) of drying due to RWU (solid lines), followed by 120 days of rewetting due to 5 mm rainfall (dashed lines).

Simulation 4: mobilised root reinforcement

Figure 5 contrasts the vertical displacement of the soil surface where the mechanical reinforcement effect of the roots is neglected (simulation 1), with simulation 4, in which it is included. The root tension resists re-expansion of the wetting soil, giving rise to a smaller upward movement of the soil surface over the final 120 days of the simulation.

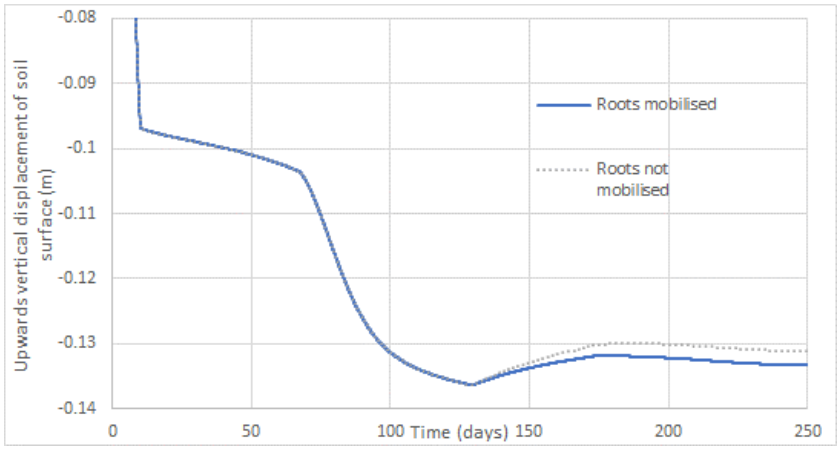

Figure 5: Vertical displacement of the soil surface for Simulation 4 where root strength is mobilised. The unmobilised simulation has otherwise identical parameters, but with zero root stiffness (i.e. E_r=0).

6 Conclusions

Given that water-soil-root interactions are potentially very significant, detailed simulation of vegetated slopes will require a coupled approach that includes physically realistic root water uptake dynamics. To achieve this, a new physically-based macroscopic model for vegetated soils has been introduced, characterised by well-established parameters that are relatively straightforward to measure. On the basis of the simulations presented, the following conclusions may be drawn.

1. Root water uptake may lower the pore water pressure sufficiently for the associated change in effective stress to cause finite strain in the soil. This implies that a linear-elastic model or an assumption of infinitesimal strain should be adopted with caution when modelling the mechanical behaviour of the rooted zone.
2. For the clayey silty sand modelled, permeability is dominated by the degree of water saturation, not by deformation (reduction in void ratio).
3. For the conditions simulated, air pressure changes make little difference to the estimated pore water pressure changes and soil deformations caused by root water uptake and rewetting by rainfall. It may be expedient (in terms of computational efficiency) to assume that the air phase remains at constant pressure.
4. For situations where there is soil expansion or shear, the stress carried by the roots may be included via a root stress tensor (which will be a function of stress and strain) to provide a rigorous basis for making improved predictions of the behaviour of vegetated slopes.

Acknowledgements

This research was funded by UK Engineering and Physical Sciences Research Council (EPSRC) grant 'Rooting for Sustainable Performance' (EPSRC EP/M020177/1 & EP/M020355/1). T.R. is funded by BBSRC SARISA BB/L025620/1, EPSRC EP/M020355/1, BBSRC SARIC BB/P004180/1, NERC NE/L00237/1 and ERC Consolidator Grant DIMR-646809. David Muir Wood and Glyn Bengough are thanked for helpful comments on the model.

Amit Patil from COMSOL is thanked for his help in remedying discrepancies we found in the Modified Cam-Clay code (the corrections will appear in version 5.5).

References

1. Wilkinson, P., et al., *An integrated hydrological model for rain-induced landslide prediction.* Earth Surface Processes and Landforms, 2002. **27**(12): p. 1285-1297.
2. Zhu, H. and L.M. Zhang, *Evaluating suction profile in a vegetated slope considering uncertainty in transpiration.* Computers and Geotechnics, 2015. **63**: p. 112–120.
3. Switala, B.M. and W. Wu, *Numerical modelling of rainfall-induced instability of vegetated slopes.* Geotechnique, 2017.
4. Ni, J.J., et al., *Modelling hydro-mechanical reinforcements of plants to slope stability.* Computers and Geotechnics, 2018. **95**: p. 99-109.
5. Morgan, R. and R. Rickson, eds. *Slope stabilization erosion control. A bioengineering approach.* 1995, E and FN Spon: London.
6. Gray, D.H. and R.B. Sotir, *Biotechnical and soil bioengineering slope stabilization.* 1996, New York: John Wiley and Sons.
7. Greenwood, J.R., et al., *Bioengineering. The Longham Wood cutting field trial* 2001, CIRIA: London.
8. MacNeil, D.J., et al., *Vegetation for slope stability*. 2001, Quality Services, Civil Engineering, Highways Agency.
9. Stokes, A., et al., *Desirable plant root traits for protecting natural and engineered slopes against landslides.* Plant Soil, 2009. **324**: p. 1-30.
10. Ollauri, A.G. and S.B. Mickovski, *Plant-Best: A novel plant selection tool for slope protection.* Ecological Engineering, 2017a. **106**: p. 154–173.
11. Greenwood, J.R., J.E. Norris, and J. Wint, *Assessing the contribution of vegetation to slope stability.* Proceedings of the Institution of Civil Engineers Geotechnical Engineering, 2004. **GE4**(Paper 13724): p. 199-207.
12. Liang, T., et al., *Scaling of the reinforcement of soil slopes by living plants in a geotechnical centrifuge.* Ecological Engineering, 2017. **109**: p. 207–227.
13. Fan, C.C. and C.F. Su, *Role of roots in the shear strength of root-reinforced soils with high moisture content. .* Ecological Engineering, 2008. **33**: p. 157–166.
14. Wu, T.H., W.P. McKinnell, and D.N. Swanston, *Strength of tree roots and landslides on Prince of Wales Island, Alaska.* Can. Geotech. J, 1979. **16**(19-33).
15. Wu, T.H., *Root reinforcement of soil: review of analytical models, test results, and applications to design.* Can. Geotech. J., 2013. **50**: p. 259–274.
16. Smethurst, J.A., D. Clarke, and W. Powrie, *Factors controlling the seasonal variation in soil water content and pore water pressures within a lightly vegetated clay slope.* Géotechnique, 2012. **62**(5): p. 429-446.
17. Briggs, K., F. Loveridge, and S. Glendinning, *Failures in transport infrastructure embankments. .* Engineering Geology., 2016. **219**: p. 107-117.
18. Scott, J.M. *Influence of vegetation on the performance of railway embankments*. in *Proceedings of the 17th European, Young Geotechnical Engineers Conference*. 2006. Zagreb, Croatia: Croatian Geotechnical Society, Velika Gorica
19. Smethurst, J.A., et al., *Mechanical and hydrological impacts of tree removal on a clay fill railway embankment.* Geotechnique, 2015. **65**(11): p. 869–882.
20. Sonnenberg, R., et al., *Centrifuge modelling of soil slopes containing model plant roots.* Can. Geotech. J., 2012. **49**: p. 1-17.
21. Doussan, C., L. Pages, and G. Vercambre, *Modelling of the hydraulic architecture of root systems: an integrated approach to water absorption—model description.* Annals of Botony, 1998. **81**: p. 213–223.
22. Rees, S.W. and N. Ali, *Seasonal water uptake near trees: a numerical and experimental study.* Geomechanics and Geoengineering. An International Journal, 2006. **1**(2): p. 129-138.
23. Karim, M.R., et al., *A rational approach for modelling the meteorologically induced pore water pressure in infrastructure slopes.* European Journal of Environmental and Civil Engineering, 2019.
24. Rouainia, M., et al., *Numerical modelling of climate effects on slope stability.* Engineering Sustainability, 2009. **162**(2): p. 81089.

25. Tsiampousi, A., L. Zdravkovic, and D.M. Potts, *Numerical study of the effect of soil–atmosphere interaction on the stability and serviceability of cut slopes in London clay.* Can. Geotech. J. , 2017. **54**: p. 405–418
26. Roscoe, K.H. and J.B. Burland, *On the generalized stress–strain behaviour of 'wet' clay.*, in *Engineering plasticity*, J. Heyman and F.A. Leckie, Editors. 1968, Cambridge University Press: Cambridge, UK. p. 535–609.
27. Muir Wood, D., *Soil Behaviour and critical state soil Mechanics.* . 1990: Cambridge University Press.
28. Mickovski, S.B., et al., *Mechanical Reinforcement of Soil by Willow Roots: Impacts of Root Properties and Root Failure Mechanism.* Soil Sci. Soc. Am. J. , 2009. **73**: p. 1276-1285.
29. Waldron, L.J., *The shear resistance of root-permeated homogeneous and stratified soil.* Soil Science Society of America Journal, 1977. **41**: p. 343–349.
30. Mao, Z., et al., *Three dimensional modelling of slope stability in heterogenous montane forest ecosystems.* Ecological Modelling, 2014. **273**: p. 11-22.
31. Bischetti, G.B., et al., *Root cohesion of forestspecies in the Italian Alps.* . Plant Soil, 2009. **324**: p. 71-89.
32. Pollen, N. and A. Simon, *Estimating the mechanical effects of riparian vegetation on stream bank stability using a fiber bundle model.* Water Resources Research, 2005. **41**(W07025).
33. Schwarz, M., P. Lehmann, and D. Or, *Quantifying lateral root reinforcement in steep slopes – from a bundle of roots to tree stands.* Earth Surface Processes and Landforms, 2010. **35**(3): p. 354-367.
34. Liang, T., J.A. Knappett, and N. Duckett, *Modelling the seismic performance ofrooted slopes from individual root–soil interaction to global slope behaviour.* Géotechnique, 2015. **65**: p. 995–1009.
35. Świtała, B.M., et al., *Experimental validation of a coupled hydro-mechanical model for vegetated soil* Geotechnique, 2018. **68**(5): p. 375-385.
36. Diambra, A., et al., *Fibre reinforced sands: experiments and modelling.* . Geotextiles and Geomembranes, 2010. **28**(3): p. 238-250.
37. Ajayi, O., et al., *A behavioural framework for fibre-reinforced gravel.* Geotechnique, 2017. **67**(1): p. 56-68.
38. Meijer, G.J., et al., *A constitutive modelling approach for root-reinforcement.* In preparation, 2019.
39. Bechmann, M., et al., *Effect of parameter choice in root water uptake models – the arrangement of root hydraulic properties within the root architecture affects dynamics and efficiency of root water uptake.* Hydrol. Earth Syst. Sci, 2014. **18**: p. 4189–4206.
40. Chen, K.P., *Hydraulic resistance of a plant root to water-uptake: a slender-body theory.* Journal of Theoretical Biology, 2016. **396**: p. 63–74.
41. Clausnitzer, V. and J.V. Hopmans, *Simultaneous modelling of transient three-dimensional root growth and soil water flow.* Plant Soil Sci., 1994. **164**: p. 299–314.
42. Doussan, C., et al., *Water uptake by plant roots: II – Modelling of water transfer in the soil root-system with explicit account of flow within the root system – Comparison with experiments.* Plant and Soil, 2006. **283**: p. 99–117.
43. Dunbabin, V.M., et al., *Modelling the interactions between water and nutrient uptake and root growth.* Plant Soil, 2002. **239**: p. 19-38.
44. Pages, L., M.O. Jordan, and D. Picard, *A simulation model of the three-dimensional architecture of the maize root system.* Plant and Soil 1989. **119**: p. 147-154.
45. Philip, J.R., *The physical principles of soil water movement during the irrigation cycle.*, in *3rd International Congression on Irrigation and Drainage*. 1957: SanFrancisco,. p. 125–154.
46. Rowse, H.R., D.A. Stone, and A. Gerwitz, *Simulation of the water distribution in soil. II. The model for cropped soil and its comparison with experiment.* . Plant Soil, 1978. **49**: p. 533–550.
47. Koebernick, N., et al., *Unraveling the hydrodynamics of split root water uptake experiments using CT scanned root architectures and three dimensional flow simulations.* Frontiers in Plant Science, 2015. **6**.
48. de Jong van Lier, Q., et al., *Modeling Water Potentials and Flows in the Soil–Plant System Comparing Hydraulic Resistances and Transpiration Reduction Functions.* 2013.
49. de Jong Van Lier, Q., et al., *Macroscopic root water uptake distribution using a matric flux potential approach.* Vadose Zone Journal, 2008. **7**: p. 1065–1078.
50. Hillel, D., H. Talpaz, and H. Van Keulen, *A macroscopic model of water uptake by a nonuniform root system and of water and salt movement in the soil profile.* Soil Science, 1976. **121**: p. 242-255.
51. Borg, H. and D. Grimes, *Depth development of roots with time: an empirical description.* Trans. ASAE, 1986. **29**(1): p. 194-197.

52. Bengough, A.G., *Modelling Rooting Depth and Soil Strength in a Drying Soil Profile.* Journal of Theoretical Biology, 1997. **186**: p. 327-338.
53. Feddes, R.A., P.J. Kowalik, and H. Zaradny, *Simulation of Field Water Use and Crop Yield, Simulation Monograph.* 1978: Pudoc, Wageningen.
54. Indraratna, B., B. Fatahi, and H. Khabbaz, *Numerical analysis of matric suction effects of tree roots. .* Proceedings of the Institution of Civil Engineerings. Geotechnical Engineering, 2006. **159**(2): p. 77–90.
55. Couvreur, V., J. Vanderborght, and M. Javaux, *A simple threedimensional macroscopic root water uptake model based on the hydraulic architecture approach.* Hydrol. Earth Syst. Sci, 2012. **16**: p. 2957–2971.
56. Javis, N., *Simple physics-based models of compensatory plant water uptake: concepts and eco-hydrological consequences.* Hydrol. Earth Syst. Sci, 2011. **15**: p. 3431–3446.
57. Siqueira, M., G. Katul, and A. Porporato, *Onset of water stress, hysteresis in plant conductance, and hydraulic lift: Scaling soil water dynamics from millimeters to meters.* Water Resources Research, 2008. **VOL. 44**(W01432).
58. Roose, T. and A.C. Fowler, *A model for water uptake by plant roots.* Journal of Theoretical Biololgy, 2004. **228**: p. 155–171.
59. Molz, F.J., *Models of water transport in the soil–plant system.* Water Resources Research, 1981. **17**(1245–1260).
60. Steudle, E. and C.A. Peterson, *How does water get through roots?* J. Exp. Bot, 1998. **49**: p. 775–788.
61. Kim, Y.X., et al., *Composite Transport Model and Water and Solute Transport across Plant Roots: An Update.* Frontiers in Plant Science, 2018. **9**(193).
62. Javot, H. and C. Maurel, *The role of aquaporins in root water uptake. .* Annals of Botony, 2002. **90**: p. 301–313.
63. Roose, T. and A.C. Fowler, *A mathematical model for water and nutrient uptake by plant root systems.* Journal of Theoretical Biology, 2004. **228**: p. 173-184.
64. Frensch, J. and E. Steudle, *Axial and radial hydraulic resistance to roots of maize (Zea mays l.).* Plant Physiol., 1989. **91**: p. 719–726.
65. Temgouaa, A.G.T., et al., *A 3D model applied to analyze the mechanical stability of real-world forested hillslopes prone to landslides.* Ecological Engineering, 2017. **106**: p. 609–619.
66. Daly, K.R. and T. Roose, *Determination of macro-scale soil properties from X-ray Computed Tomography: Model derivation.* Proceedings of the Royal Society A. Mathematical, Physical and Engineering Sciences, 2018. **474**(2209).
67. Laloui, L., M. Nuth, and B. Francois, *Mechanics of unsaturated soils*, in *Mechanics of unsaturated geomaterials*, L. Laloui, Editor. 2010, ISTE Ltd: Great Britain.
68. Hackett, *Hyperelasticity Primer.* 2016: Springer.
69. Coussy, O., *Mechanics and Physics of Porous Solids*. 2010.
70. McMinn, C.W., E.R. Dufresne, and J.S. Wettlaufer, *Large deformations of a soft porous material. .* Physical Review Applied, 2016. **5**: p. 044020.
71. Van Genuchten, M.T., *A closed-form equation for predicting the hydraulic conductivity of unsaturated soils.* Soil Sci. Soc. Am., 1980. **44**: p. 892–898.
72. Parker, J.C., R.J. Lenhard, and T. Kappusamy, *A parametric model for constitutive properties governing multiphase flow in porous media. .* Water Resources Research, 1987. **4**: p. 618-624.
73. Al-Tabbaa, A. and D. Muir Wood, *Some measurements of the permeability of kaolin.* Geotechnique, 1987. **37**(4): p. 499-514.
74. Chapuis, R.P. and M. Aubertin, *On the Use of the Kozeny–Carman Equation to Predict the Hydraulic Conductivity of Soils.* Canadian Geotechnical Journal, 2011. **40**: p. 616-628.
75. Landsberg, J.J. and N.D. Fowkes, *Water movement through plant roots.* Ann. Bot., 1978. **42**: p. 493–508.
76. Bishop, A.W. and G.E. Blight, *Some Aspects of Effective Stress in Saturated and Partly Saturated Soils* Geotechnique, 1963. **13**(3): p. 177-197.
77. Vanapalli, S.K. and D.G. Fredlund, *Comparison of Different Procedures to Predict Unsaturated Soil Shear Strength* in *Geo-Denver*, C. Shackleford, S.L. Houston, and N.-Y. Chang, Editors. 2000, ASCE: Denver, Colorado, United States
78. Houlsby, G.T., *The work input to an unsaturated granular material.* Geotechnique, 1997. **47**

p. 193-196.

79. Nuth, M. and L. Laloui, *Effective stress concept in unsaturated soils: clarification and validation of a unified framework.* International Journal for Numerical and Analytical Methods in Geomechanics, 2008. **32**: p. 771-801.
80. Lu, N. and D.V. Griffiths, *Profiles of Steady-State Suction Stress in Unsaturated Soils.* JOURNAL OF GEOTECHNICAL AND GEOENVIRONMENTAL ENGINEERING, 2004. **130**(10): p. 1063-1076.
81. AB, C., *COMSOL Multiphysics® v. 5.3a.* . 2016: Stockholm, Sweden.
82. Tuzet, A., A. Perrier, and R. Leuning, *A coupled model of stomatal conductance, photosynthesis and transpiration.* Plant, Cell and Environment, 2003. **26**: p. 1097–1116.
83. Heppell, J., et al., *Validation of a spatial–temporal soil water movement and plant water uptake model.* Geotechnique, 2014. **64**(7): p. 526–539.
84. Meijer, G., et al., *In situ measurement of root reinforcement using corkscrew extraction method. .* Canadian Geotechnical Journal, 2018. **55**(10): p. 1372-1390.
85. North, G.B. and P.S. Nobel, *Radial hydraulic conductivity of individual root tissues of Opuntia ficus-indica (L) Miller as soil moisture varies. .* Annals of Botony, 1996. **77**: p. 133–142.
86. Smethurst, J.A., D. Clarke, and W. Powrie, *Seasonal changes in pore water pressure in a grass-covered cut slope in London Clay.* Geotechnique, 2006. **56**(8): p. 523–537.
87. Gibson, R.E., G.L. England, and M.J.L. Hussey, *The Theory of One-Dimensional Consolidation of Saturated Clays. 1. Finite Non-Linear Consildation of Thin Homogeneous Layers* Geotechnique, 1967. **17**(3): p. 261-273.

Supplement A: Lagrangian Equations

The system of equations [1-24] given in the main text are all in Eulerian co-ordinates, *i.e.*, relative to a fixed spatial reference frame. As the solid deforms the shape of the solid changes; particles comprising the material move in space, as do non-fixed boundaries. Therefore, a numerical solution to the equations in Eulerian co-ordinates will require moving boundaries and mesh. It is instead convenient to solve the equations of the solid in a Lagrangian (material) reference frame together with spatially-fixed boundary conditions in the Lagrangian frame. This requires a series of conversions, which are set out in this supplement.

Nominal (Lagrangian) volume fractions (Coussy, 2004, 2010; McMinn *et al.*, 2016) are defined as:

$$\Phi_s = \phi_s(x,0) = \phi_{s,0} = J\phi_s, \quad \text{[A1]}$$

$$\Phi_w = J\phi_w, \quad \text{[A2]}$$

$$\Phi_a = J\phi_a, \quad \text{[A3]}$$

$$\Phi_a + \Phi_w + \Phi_s = J, \quad \text{[A4]}$$

where, $\Phi_s = \Phi_{so} + \Phi_r$ and the Eulerian volume fractions for the solid, water, air and roots are ϕ_s, ϕ_w, ϕ_a and ϕ_r respectively.

Recall equation [7] from the main text in Eulerian coordinates is given by

$$\frac{\partial \phi_w}{\partial t} + \nabla.\left[-\frac{k}{\mu}\left(\nabla p_w + \rho g\widehat{\boldsymbol{k}}\right)\right] + \nabla.(\phi_w \boldsymbol{v_s}) = -F_R, \quad \text{[A5]}$$

which is more succinctly expressed as:

$$\frac{\partial \phi_w}{\partial t} + \nabla.(\boldsymbol{q_w}) = -F_R. \quad \text{[A6]}$$

The divergence is converted by $\frac{1}{J}\nabla_X.\boldsymbol{T_0} = \nabla.\boldsymbol{T}$ (this can be shown using the Piola Transformation and making using of the divergence theorem). Volume quantities are transformed, by scaling by J, for instance, $\Phi_w = J\phi_w$. Flux quantities are converted by pre-multiplying by $J\boldsymbol{F^{-1}}$, i.e. $W_w = J\boldsymbol{F^{-1}}\boldsymbol{q}$ (and note, $\boldsymbol{q}$ is a column-vector).

Thus, converting equation (A6) into Lagrangian water content Φ_w and flux $\boldsymbol{W_w}$ gives:

$$\frac{1}{J}\frac{\partial \Phi_w}{\partial t} + \frac{1}{J}\nabla_X.(\boldsymbol{W_w}) = -\frac{1}{J}F_R,$$

$$\frac{\partial \Phi_w}{\partial t} + \nabla_X.(\boldsymbol{W_w}) = -F_R. \quad \text{[A7]}$$

For the Darcy component, the solid velocity v_s is zero in Lagrangian co-ordinates. To convert the pressure gradient (which is given as a column vector), the Eulerian gradient ∇ is replaced by $\boldsymbol{F^{-T}}\nabla_X$ (this arises from the Piola transformation and Nanson's formula). Thus, the conversion proceeds as:

$$\phi_w(\boldsymbol{v_w} - \boldsymbol{v_s}) = -\frac{k}{\mu}\left(\nabla p_w + \rho g\widehat{\boldsymbol{k}}\right),$$

$$(q_w - \phi_w \boldsymbol{v_s}) = -\frac{k}{\mu}\left(\nabla p_w + \rho g\widehat{\boldsymbol{k}}\right),$$

$$\frac{1}{J}F\boldsymbol{W_w} = -\frac{k}{\mu}\boldsymbol{F^{-T}}\left(\nabla_X p_w + \rho g\widehat{\boldsymbol{k}}\right),$$

$$\boldsymbol{W_w} = -\frac{k}{\mu}\boldsymbol{JF^{-1}F^{-T}}\left(\nabla_X p_w + \rho g\widehat{\boldsymbol{k}}\right),$$

$$\boldsymbol{W_w} = -\frac{k}{\mu}\boldsymbol{JC^{-1}}\left(\nabla_X p_w + \rho g\widehat{\boldsymbol{k}}\right). \quad [A8]$$

The procedure is applied in a similar fashion for the air phase conservation:

$$\frac{\partial\phi_a}{\partial t} + \nabla.\left[-\frac{k_a}{\mu_a}\left(\nabla p_a + \rho_a g\hat{k}\right)\right] + \nabla.[\boldsymbol{v_s}\phi_a] = 0, \quad [A9]$$

$$\frac{\partial\phi_a}{\partial t} + \nabla.(\phi_a\boldsymbol{v_a}) = 0. \quad [A10]$$

Converting [A10] to Lagrangian frame results in:

$$\frac{\partial\Phi_a}{\partial t} + \nabla_X.(\boldsymbol{W_a}) = 0. \quad [A11]$$

Converting Darcy's law gives:

$$\boldsymbol{W_a} = -\frac{k_a}{\mu_a}\boldsymbol{JF^{-1}F^{-T}}\left(\nabla_X p_a + \rho_a g\widehat{\boldsymbol{k}}\right),$$

$$\boldsymbol{W_a} = -\frac{k_a}{\mu_a}\boldsymbol{JC^{-1}}\left(\nabla_X p_a + \rho_a g\widehat{\boldsymbol{k}}\right), \quad [A12]$$

where $\boldsymbol{C^{-1}} = \boldsymbol{F^{-1}F^{-T}}$ is the Piola deformation tensor (which is the inverse of the Cauchy-Right Tensor).

Converting the force equilibrium equation:

$$\nabla.\boldsymbol{\sigma} = -\boldsymbol{f_v},$$

by using, the Piola Transformation, such that $\frac{1}{J}\nabla_X.\boldsymbol{T_0} = \nabla.\boldsymbol{T}$ and $\boldsymbol{T_0} = \boldsymbol{JTF^{-T}}$, giving:

$$\boldsymbol{F_V} + \nabla_X.\boldsymbol{\sigma JF^{-T}} = 0,$$

$$\boldsymbol{F_V} + \nabla_X.\boldsymbol{FF^{-1}\sigma JF^{-T}} = 0,$$

$$\boldsymbol{F_V} + \nabla_X.(F\boldsymbol{\sigma_2}) = 0,$$

where $\nabla_X \equiv \frac{\partial}{\partial X_i}.(\cdot)$ is written to distinguish it from the operator $\nabla.(\cdot) \equiv \frac{\partial}{\partial x_i}.(\cdot)$. The stress measure $\boldsymbol{\sigma_2} = \boldsymbol{F^{-1}\sigma JF^{-T}}$ is defined as the second Piola-Kirchhoff stress tensor. It is symmetric and is a function of only material co-ordinates. Thus:

$$\nabla_X.(\boldsymbol{F\sigma_2}) = -\boldsymbol{F_V}. \quad [A13]$$

For the elastic law, the Lagrangian stress-strain pair that is conjugate with the Eulerian elastic law in Equation [20] is simply (Hackett, 2016):

$$\boldsymbol{\sigma_2}' = \boldsymbol{C}:\boldsymbol{\varepsilon_{GL}},$$

$$\boldsymbol{F^{-1}\sigma JF^{-T}} = \boldsymbol{C}:\boldsymbol{\varepsilon_{GL}}, \quad [A14]$$

where the Green-Lagrange strain, $\boldsymbol{\varepsilon_{GL}} = \frac{1}{2}(\boldsymbol{F^TF} - I)$.

(Noting that elastic and plastic strains relate via the multiplicative strain decomposition, $\boldsymbol{F_e} = \boldsymbol{FF_p^{-1}}$). Thus, the linear-elastic law is cast in Lagrangian co-ordinates as:

$$\nabla_X.\left(\boldsymbol{\sigma_2}(\boldsymbol{X})\right) = \nabla_X.\{(J-\Phi_r)[\boldsymbol{C}:\boldsymbol{\varepsilon_{GL}}(\boldsymbol{X}) + p_w(\boldsymbol{X})J\boldsymbol{F}^{-T}S_w(\boldsymbol{X})I + p_a(\boldsymbol{X})J\boldsymbol{F}^{-T}(1-S_w(\boldsymbol{X}))I] + \Phi_r J\boldsymbol{F}^{-T}\boldsymbol{\sigma_r}\} = -\boldsymbol{F_V}(\boldsymbol{X}) \quad \text{[A15]}$$

The simple root model used for demonstration in this paper is based on an 'intermediate' deformation of the soil, $\boldsymbol{F_1}$, defined at a particular point in time (t_r). This allows for the simulation necessity of first consolidating the soil with body forces and then potentially applying other deformations before the root is assumed to be mechanically 'set'; i.e. ready to withstand tension.

The total deformation at time ($t > t_r$) is given by $\boldsymbol{F} = \boldsymbol{F_2}\boldsymbol{F_1}$, where $\boldsymbol{F_2}$ is the deformation relative to the intermediate state. Thus, the change in strain due to deformation from the intermediate state is $\boldsymbol{\varepsilon^*_{GL}} = \frac{1}{2}\left(\boldsymbol{F_2^T F_2} - I\right)$. So, of course, at $t = t_r$, $\boldsymbol{\varepsilon'_{GL}} = 0$.

A linear relationship between vertical tension and strain is defined in this intermediate frame, i.e. $\boldsymbol{\sigma^*_{2r,zz}} = E_r \mathrm{Max}\left[0, \boldsymbol{\varepsilon^*_{GL,zz}}\right]$, whilst all other root stress components are assumed to be zero, i.e. $\boldsymbol{\sigma_{2r,(i,j)}} = 0$.

The root stress tensor $\boldsymbol{\sigma_r}$ in the original reference frame was found by transforming the root stress tensor $\boldsymbol{\sigma^*_{2r,zz}}$ back into the reference configuration: $\boldsymbol{\sigma_{2r,zz}} = \det(\boldsymbol{F_1})\boldsymbol{F_1^{-1}}\boldsymbol{\sigma^*_{2r,zz}}\boldsymbol{F_1^{-T}}$

The saturations are also expressed in nominal porosities, *i.e.*:

$$S_w = \frac{\Phi_w}{\Phi_w + \Phi_a} = \frac{\Phi_w}{J - \Phi_s}, \quad \text{[A16]}$$

$$S_a = \frac{\Phi_a}{J - \Phi_s}. \quad \text{[A17]}$$

So:

$$S_w + S_a = 1. \quad \text{[A18]}$$

Converting the root uptake rate is analogous to equation A7 where the Js cancel. Thus,

$$\pi d_r k_R (p_w - p_R) = -\frac{\partial}{\partial Z}\left[k_z\left(\frac{\partial p_R}{\partial Z} + \rho g \widehat{\boldsymbol{k}}\right)\right]. \quad \text{[A19]}$$

The Lagrangian equations are given in Table S1 next to the Eulerian equations.

Table S1: Summary of model in Eulerian and Lagrangian reference frames

Description [equation number in main text and in this supplementary]	Eulerian	Lagrangian
Water flow [7 ,A5]	$\frac{\partial \phi_w}{\partial t} + \nabla.\left[-\frac{k}{\mu}\left(\nabla p_w + \rho g \widehat{\boldsymbol{k}}\right)\right] + \nabla.(\boldsymbol{v_s}\phi_w) = -F_R$	$\frac{\partial \Phi_w}{\partial t} + \nabla_X.\left(-\frac{k}{\mu} J\boldsymbol{C^{-1}}\nabla_X p_w + \rho g \widehat{\boldsymbol{k}}\right) = -\boldsymbol{F_R}$
Air flow [8, A8]	$\frac{\partial \phi_a}{\partial t} + \nabla.\left[-\frac{k_a}{\mu_a}\left(\nabla p_a + \rho_a g \widehat{\boldsymbol{k}}\right)\right] + \nabla.[\boldsymbol{v_s}\phi_a] = 0$	$\frac{\partial \Phi_a}{\partial t} + \nabla_X.\left(-\frac{k_a}{\mu_a} J\boldsymbol{C^{-1}}\nabla_X p_a + \rho_a g \widehat{\boldsymbol{k}}\right) = 0$
Force equilibrium and constitutive elastic law [20, A15]	$\nabla.\boldsymbol{\sigma} = \nabla.\{(1-\phi_r)[\boldsymbol{C}:\boldsymbol{\varepsilon_e} + p_w S_w I + p_a(1-S_w)I] + \phi_r \boldsymbol{\sigma_r}\} = -\boldsymbol{f_v}$	$\nabla_X.(\boldsymbol{\sigma_2}(\boldsymbol{X})) = \nabla_X.\{(J-\Phi_r)[\boldsymbol{C}:\boldsymbol{\varepsilon_{GL}}(\boldsymbol{X}) + p_w(\boldsymbol{X})J\boldsymbol{F^{-T}}S_w(\boldsymbol{X})I + p_a(\boldsymbol{X})J\boldsymbol{F^{-T}}(1-S_w(\boldsymbol{X}))I] + \Phi_r J\boldsymbol{F^{-T}}\boldsymbol{\sigma_r}\} = -\boldsymbol{F_V}(\boldsymbol{X})$
Strain [19, -]	$\boldsymbol{\varepsilon} = \frac{1}{2}(I - \boldsymbol{F^T F^{-1}})$	$\boldsymbol{\varepsilon_{GL}} = \frac{1}{2}(\boldsymbol{F^T F} - I)$
Water retention / saturation [9, A16]	$S_w = \frac{\phi_w}{1-\phi_s} = \frac{1}{\left[1+\left(\frac{\alpha(p_a-p_w)}{\rho g}\right)^N\right]^M}$	$S_w = \frac{\Phi_w}{\Phi_w+\Phi_a} = \frac{\Phi_w}{J-\Phi_s} = \frac{1}{\left[1+\left(\frac{\alpha(p_a-p_w)}{\rho g}\right)^N\right]^M}$
Solid velocity [4 ,-]	$\boldsymbol{v_s} = F.\left.\frac{\partial u}{\partial t}\right\|_x$	0
Solid volume fraction [2, A1]	$\phi_s = \frac{\phi_{s,0}}{J}$	$\Phi_s = \phi_s(x,0) = \phi_{s,0} = J\phi_s$
Water volume fraction [- ,A2]	$\phi_w = S_w\left(1-\frac{\phi_{s,0}}{J}\right)$	$\Phi_w = S_w(J-\Phi_s)$
Air volume fraction [- ,A3]	$\phi_a = 1 - \frac{\left(1-\frac{\phi_{s,0}}{J}\right)}{\left[1+\left(\frac{\alpha(p_a-p)}{\rho g}\right)^N\right]^M} - \frac{\phi_{s,0}}{J}$	$\Phi_a = J - \Phi_w - \Phi_s$
Root pressure [14 ,A19]	$\pi d_r k_R(p_w - p_R) = -\frac{\partial}{\partial Z}\left[k_z\left(\frac{\partial p_R}{\partial Z} + \rho g \widehat{\boldsymbol{k}}\right)\right]$	$\pi d_r k_R(p_w - p_R) = -\frac{\partial}{\partial Z}\left[k_z\left(\frac{\partial p_R}{\partial Z} + \rho g \widehat{\boldsymbol{k}}\right)\right]$

Supplement B – Verification

In this supplement, (A) simple drainage in the absence of root water uptake is used to verify the water-flow aspect of the model in comparison to Richards equation and (B) a range of root uptake parameters are used to validate the root water uptake (RWU) aspect of the model in comparison to analytical solutions. In both simulations, unless otherwise indicated all conditions are the same as for Simulation 1 and parameters are as given in Table 1 of the main text. Consolidation of the soil by the gravity body force is omitted for the purpose of validation.

A. Soil Water flow

Figure SB1 shows the water pressures and saturations obtained by simulation of the soil being drained from fully saturated without any rainfall or RWU. A drying front progresses down through the profiles, with the pressure dropping from 0 kPa at the start to around -20 kPa at the ground surface after 120 days. The pressure profile asymptotically approaches the drained-hydrostatic line from the base upwards. The pressure and saturation profiles from the model are validated by a close match to the results obtained by independently applying Richards' Equation. The saturation profiles are mapped from the pressure profiles.

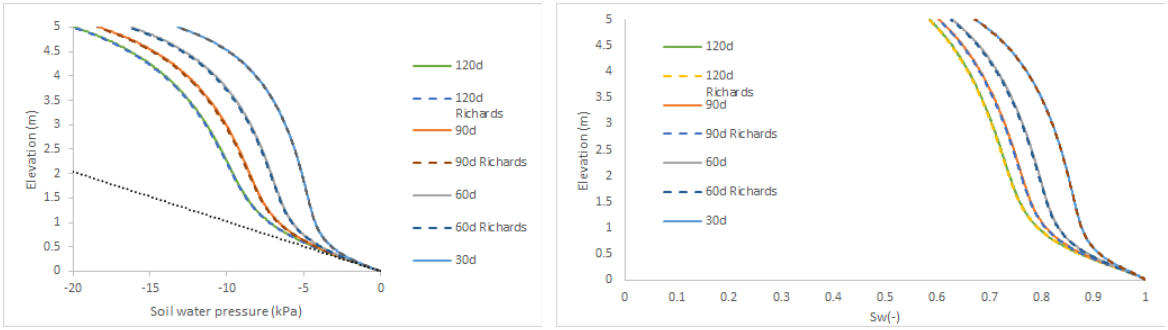

Figure SB1: Drain-down from saturation, for linear-elastic soil at 30, 60, 90 and 120 d, where the y-axis is the elevation of the soil column. Parameters from Table 1 in main text were used, with $R = 0$ mm/d and without any body-force applied to the soil. Notice that the scale for the pressure has a range from 0 to -20 kPa, whereas for the remaining figures the scale is 0 to -1000 kPa. Dashed lines give the solutions from Richards Equation (solved using COMSOL 5.2a subsurface flow module).

B. Xylem flow

To test the RWU term, the same conditions as for Simulation 1 are used except that the 10 day period of ramping the body force is omitted and the simulation is stopped before the rainfall is added so as to concentrate on the drying period.

The relative importance of the axial and radial flows to the root are given by the ratio:

$$\kappa^2 = \pi d_r k_R L^2 / k_z. \qquad [B1]$$

For k_z=1×10^{-13} m^4/s/Pa, k_R=1×10^{-14} m/s/pa, $d_r = 0.001$ m, L_R=1 m and l_d =1785 m/m^3, the result is $\kappa^2 = 0.003$ which is much less than 1. So in this case, the pressure profile in the root is expected to be close to hydrostatic. Roose & Fowler (2004) estimated an equivalent up-scaled $\kappa^2 \sim 1$, by including the contribution of first-order Maize roots. This condition is tested by reducing k_z to 1×10^{-16} m/s/Pa (i.e. $\kappa^2 = 0.3$). Then, lowering by another factor of 100, k_z=1×10^{-18} m/s/Pa is used to examine conditions under which the axial root flow component begins to dominate. Lower values of k_z are not tested since this would be considerably outside of the range of values in the literature.

For the base parameters (table 1 in main text), $\kappa^2 = 0.003$. This means that the radial root flow dominates and the pressure in the root water is very close to being hydrostatic. This is confirmed in the left-most column of Figure SB2 where the simulated root pressure, p_R, is compared to hydrostatic.

For k_z=1×10^{-16} m^4/s/Pa ($\kappa^2 = 0.3$), shown in the middle column of Figure SB2 neither radial nor axial root flow dominates. For this condition, p_R diverges from hydrostatic, and so the pattern of RWU is changed, together with the soil pressure and variables that depend on it (saturation and strain). The RWU is reduced with depth relative to the base parameter condition, albeit this is a relatively subtle change.

A more substantial alteration of the hydraulics relative to the baseline occurs for where k_z=1×10^{-18} m^4/s/Pa ($\kappa^2 = 31.4$). Here, the axial root flow dominates. Solving equation [15] for root pressure under this condition gives (Roose & Fowler, 2004):

$$p_R(z) = p(z) - [P - p(0)]e^{-\kappa z} \qquad \text{[B2]}$$

Equation [B2] is plotted on Figure SB2, giving a good match to the numerical result for k_z (thus validating the RWU aspect of the model). Examining the third column in Figure SB2 it is clear that the total RWU is significantly smaller, and with a larger proportion of the uptake coming from the upper sections of the root.

For simulation it is useful to know a priori which of these three cases applies, since applying a hydrostatic p_R or exponential does not require the root pressure equation. However, when neither conductivity is dominating, i.e. when $\kappa^2 \sim 1$, the pressure in the root must be found by solving the coupled root-pressure and soil pressure equations.

k_z=1×10^{-13} m^4/s/Pa (Set 3)	k_z=1×10^{-16} m^4/s/Pa (Set 5i)	k_z=1×10^{-18} m^4/s/Pa (Set 5ii)

$\kappa^2 = 0.003$	$\kappa^2 = 0.314$	$\kappa^2 = 31.4$
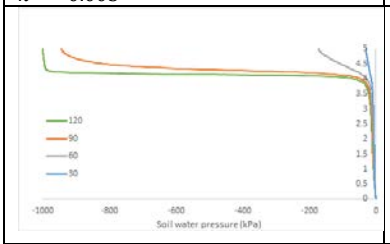	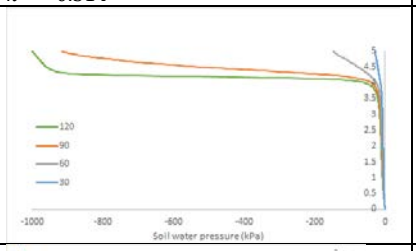	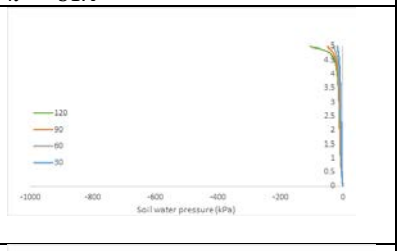
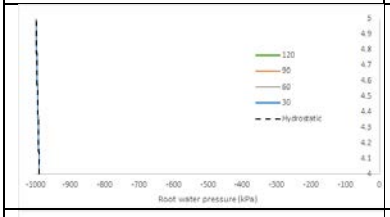	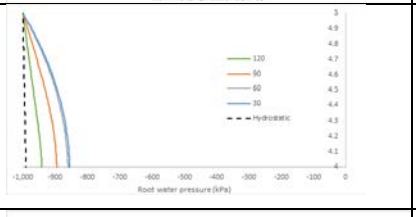	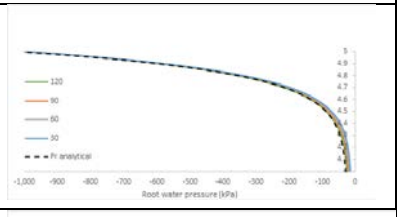
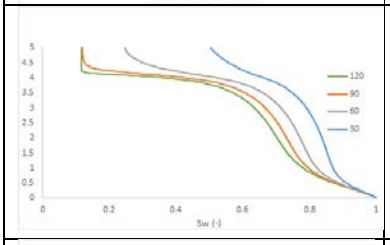	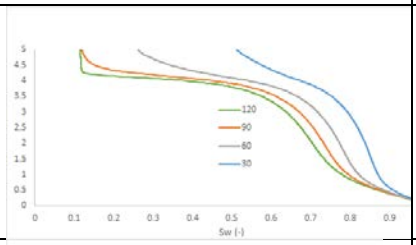	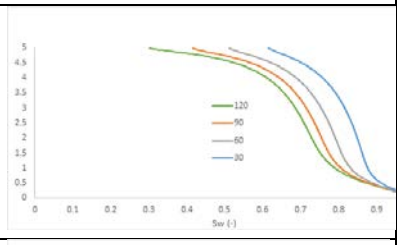
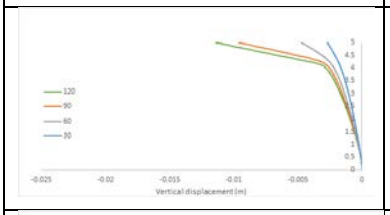	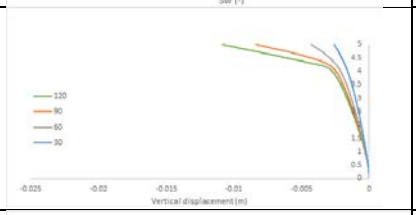	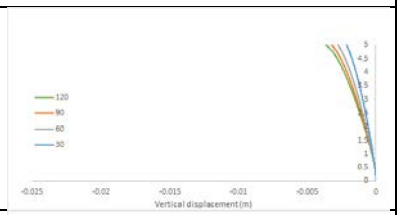
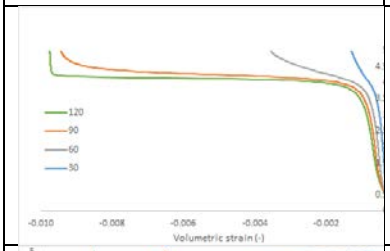	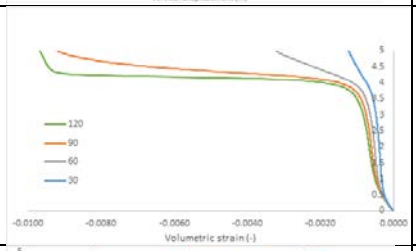	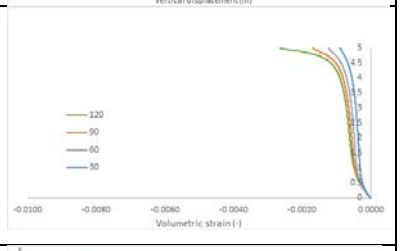
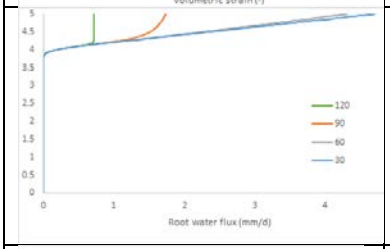	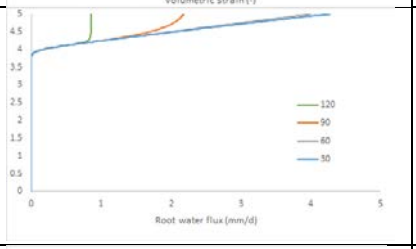	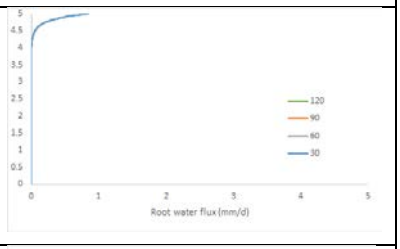
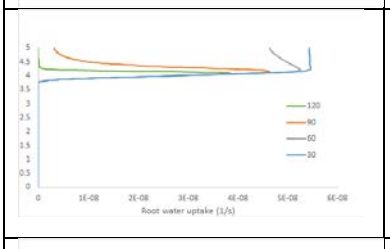	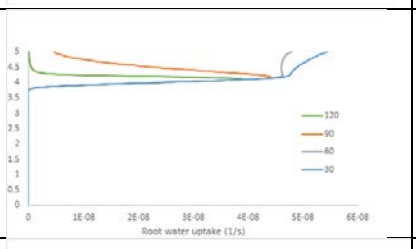	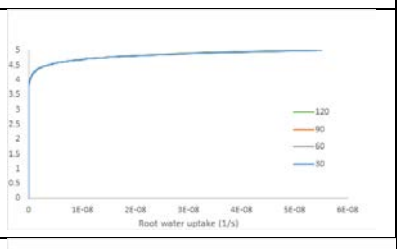
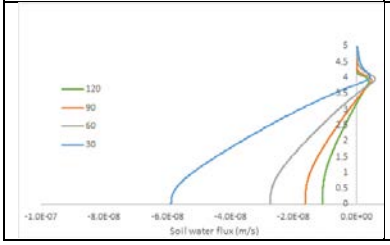	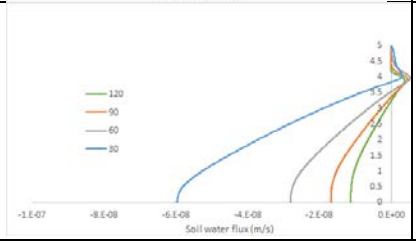	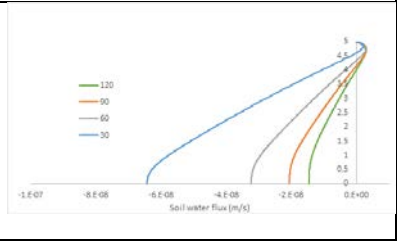

Figure SB2: Sensitivity to axial root conductance for 120 days after consolidation (times 30d, 60d, 90 and 120d shown), where the elevation in the soil column is shown on the y-axis. Parameters given in Table 1 in the main text. For k_z=1×10^{-18}, the analytical solution for p_R is given by Equation [B2]